Microstructure Evolution in Deformed and Recrystallized Electrical Steel

A Thesis

Submitted to the Faculty

of

Drexel University

by

Dejan Stojakovic

in partial fulfillment of the

requirements for the degree

of

Doctor of Philosophy

March 2008

Dedications

With love and affection to my son Filip.

Acknowledgments

Above all, I would like to thank my wife Angelina for her support and her immense patience and my family for their continuous support throughout my education.

I would like to express my profound gratitude to my advisors Prof. Roger D. Doherty and Prof. Surya R. Kalidindi for their guidance and support.

I would like to thank the committee members Prof. Alan C.W. Lau, Prof. Jonathan E. Spanier and Dr. Fred B. Fletcher for serving in my committee and providing me helpful suggestions in improving the quality of my thesis.

I am grateful to Prof. Fernando J.G. Landgraf at the University of Sao Paulo, Brazil, for providing the samples for this study and numerous discussions.

I would like to acknowledge Mr. Siddhartha Pathak for very productive collaboration in developing the nanoindentation analyses methods.

Special thanks are due to Mr. Mark Shiber for helping me with all the tooling needed for my experimental work.

I would also like to thank all the faculty and staff, especially Prof. Richard Knight and Mrs. Judith Trachtman, for providing supportive and rich environment.

I am thankful to all of my fellow graduate students for their friendly support, particularly to Mr. Christopher J. Hovanec for sharing the ups and downs.

Last, but by no means least, I thank Prof. Leposava Sidjanin at the University of Novi Sad, Serbia, for encouragement and support to continue my education in America.

The work was made possible by support of The Centralized Research Facilities at Drexel University. The research was funded by NSF (DMR0303395).

Table of Contents

LIST OF TABLES vi

LIST OF FIGURES vii

ABSTRACT x

1. INTRODUCTION 1

2. BACKGROUND 5

2.1 Deformation 5

2.2 Recrystallization 7

2.3 Microstructure and Properties 9

2.4 Experimental Techniques 12

2.5 Objective 13

3. EXPERIMENTAL METHODS 15

3.1 Crystallographic Orientation 16

3.2 Orientation Imaging Microscopy 18

3.3 Stored Energy 20

3.4 Nanoindentation 23

4. MODELING METHODS 27

4.1 Taylor Factor 27

4.2 Taylor Model 30

4.3 Finite Element Model 30

5. EXPERIMENTAL RESULTS 31

5.1 Materials 31

5.2 Rolling Experiment 33
5.2.1 Thermomechanical Processing 33
5.2.2 Crystal Plasticity Modeling 38
5.3 Nanoindentation Experiment 42
5.3.1 Zero-Displacement and Zero-Load 43
5.3.2 Indentation Taylor-like Factor 45
5.4 Plane Strain Compression Experiment 50
5.3.4 First Deformation Stage 54
5.3.5 Second Deformation Stage 57
5.4.3 Third Deformation Stage 58
5.5 Annealing Experiment 62
6. DISCUSSION 69
7. CONCLUSIONS 78
8. SUGGESTIONS FOR FUTURE WORK 80
LIST OF REFERENCES 81
APPENDIX 86
VITA 87

List of Tables

1. Chemical composition of the as-cast alloys (wt. %) 33

2. Grain sizes of as-cast structure and recrystallized structures after deformation and mean Taylor factor (M) for recrystallized structures 36

3. Extracted average indentation yield strength and average effective indentation modulus from indentation stress-strain curves for as-cast equiaxed grains 47

4. Extracted values of indentation yield strength, change in critical resolved shear stress and dislocation density after plane strain compression to true strain of 1.6 52

5. Extracted: 5a) yield strength and 5b) strain hardening from nanoindentation (NI) stress-strain curves and plane strain compression (PSC) true stress-strain curves 54

6. Extracted indentation yield strength for as-cast columnar grains 56

7. Extracted values of indentation yield strength, change in critical resolved shear stress, dislocation density and calculated strain path average Taylor factors (M_{spa}) after the first deformation stage 57

8. Extracted values of indentation yield strength, change in critical resolved shear stress, dislocation density and calculated strain path average Taylor factors (M_{spa}) after the second deformation stage 58

9. Extracted values of indentation yield strength, change in critical resolved shear stress, dislocation density and calculated strain path average Taylor factors (M_{spa}) after the third deformation stage 61

10. Extracted values of indentation yield strength, change in critical resolved shear stress, decrease in dislocation density and Taylor factor (M) after deformation followed by partial annealing in recrystallized grains 65

11. Extracted values of indentation yield strength, change in critical resolved shear stress, decrease in dislocation density and Taylor factor (M) after deformation followed by partial annealing in recovered regions 66

List of figures

1. Schematic representation of: a) preferred lambda fiber texture for AC motors, b) ϕ_2=45^o section of the Euler space with positions of lambda fiber, Goss component and the commonly developed alpha and gamma fibers on rolling in BCC iron 2

2. Schematic representation of: a) polycrystalline microstructure depicting the different orientation of the crystals, b) sample reference frame and crystal frame inside the bulk material 15

3. Schematic representation of the Bunge-Euler convention, which rotates the sample reference frame into the crystal reference frame 16

4. ODF of directionally solidified electrical steel with the lambda fiber texture 18

5. a) schematic of the sample inside the SEM chamber, b) EBSD pattern 19

6. a) Example of load-displacement curve for electrical steel, b) sketch of the primary zone of indentation for spherical indentation 26

7. Schematic of the prepared sample with the ODF plots showing lambda fiber at the top and bottom sides in the continuously cast iron-silicon alloy 31

8. Schematic of the prepared sample with the ODF plots showing lambda fiber at the top and bottom sides in the directionally solidified iron-silicon alloy 32

9. ND IPF maps of the recrystallized structures at a) surface and b) midplane after (I) the 90% reduction, (II) the first 10% reduction and (III) the second 10% reduction 35

10. ODF plots from a) surface and b) midplane after (I) the 90% reduction and after subsequent recrystallizations following (II) the 90% reduction, (III) the first 10% reduction, (IV) the second 10% reduction 36

11. Finite element mesh with C3D8 elements used in: a) cubical mesh for Taylor factor calculations and light deformation simulations, b) single-layer mesh for heavy plane strain deformation simulation of columnar grained sample 39

12. Taylor factor (M) maps for orientations on the ϕ_2 = 45^o section obtained by: a) Taylor model, b) Micromechanical finite element model 40

13. Modeled crystal rotations seen on the Φ_2 = 45^o section for 10% reduction by: a) Taylor model, b) Micromechanical finite element model 41

14. Textures of samples: a) as-cast, b) after plane strain compression experiment, c) predicted by Taylor model, d) predicted by finite element model after true strain of 1.6 42

15. New method for identification of the effective zero-point based on the straight portion of the line, shown in the plot, used to estimate zero-load and zero-displacement 44

16. Example of indentation stress-strain curves with the developed zero point correction and default zero point from the machine 45

17. a) ND IPF map of the equiaxed grain structure in as-cast state, b) standard stereographic triangle showing orientation of the grains 46

18. Example of indentation stress-strain curves a) without pop-ins, b) with pop-ins showing differences in indentation yield strength in the as-cast structure 47

19. Comparison of indentation moduli M with the Young's moduli E for three different orientations as a function of elastic constants (Young's modulus and Poisson's ratio in the cube directions) and anisotropy factor [128]. Anisotropy factor for electrical steel is calculated and extracted range for indentation moduli is in very good agreement with the experimentally obtained values....48

20. Interpolated indentation yield strength surface as a function of two Bunge-Euler angles from experimental measurements shown as the dark spheres 49

21. a) ND IPF map of the columnar grain sample after plane strain compression to true strain of 1.6, b) standard stereographic triangle showing developed orientations within the grain used for nanoindentation measurements (circled regions in the IPF map)....51

22. Extracted indentation stress-strain curves from differently oriented regions within the lambda grain deformed to true strain of 1.6 and from the initial as-cast state 53

23. True stress-strain curves for the three stages of the plane strain compression experiments to: a) true strain of 1.6, b) true strain of 1.21 54

24. ND IPF maps of the top surface showing a) as-cast microstructure, and microstructure after plane strain compression to true strain of b) 0.34, c) 0.81 and d) 1.21 55

25. ODF plots of (I) initial texture and after plane strain compression a) experiment, b) simulation to true strain of (II) 0.34, (III) 0.81 and (IV) 1.21 56

26. ND IPF maps of (I) individual grains after the third deformation step showing fragmentation of the grains with repeating orientation fields (II) close to the lambda fiber, (III) distant from the lambda fiber 59

27. Examples of the extracted indentation stress-strain curves from grain no.6 for the three deformation steps including two different deformation bands developed during the third stage (6A and 6B) 62

28. Plot of extracted dislocation density and strain path average Taylor factor 62

29. Variation of the Vickers micro-hardness in iron-silicon electrical steel, deformed in plane strain compression to true strain of 1.6, with time at 620^{o}C in salt bath 63

30. ND IPF maps of a) deformed sample, b) partially annealed sample (showing the selected recrystallized grains (circles) and well recovered regions (squares) for nanoindentation measurements) and grain boundary color maps for c) deformed sample, d) partially annealed sample with the insets showing high angle boundaries (more than 15^{o} are colored blue) surrounding selected recrystallized for nanoindentation study 64

31. Interpolated indentation yield strength surface as a function of two Bunge-Euler angles from experimental measurements (original data from as-cast structure plus data from recrystallized grains) shown as the dark spheres 66

32. Examples of the extracted indentation stress-strain curves containing pop-ins in recrystallized grain no. 3 and well recovered regions no. 3 and 5 67

33. Examples of the extracted indentation stress-strain curves without pop-ins in well recovered regions no. 1, 2 and 4 67

34. Sketch of the increase with time (left to right) of the primary indentation zone 74

35. Extracted values for indentation moduli and indentation yield strength across grain boundary between grain no.1 (on the left side) and grain no. 2 (on the right side) 86

Abstract

Microstructure Evolution in Deformed and Recrystallized Electrical Steel
Dejan Stojakovic
Roger D. Doherty, D. Phil.
Surya R. Kalidindi, Ph.D.

A processing route has been developed for recovering the desired lambda fiber in iron-silicon electrical steel needed for superior magnetic properties in electric-motor application. The lambda fiber texture is available in directionally solidified iron-silicon steel with the <001> columnar grains but was lost after heavy rolling and recrystallization required for motor laminations. Two steps of light rolling each followed by recrystallization were found to largely restore the desired fiber texture. This strengthening of the <001> fiber texture had been predicted on the basis of the strain induced boundary migration mechanism during recrystallization of lightly rolled steel from existing grains of near the ideal orientation, due to postulated low stored energies. Taylor and finite element models supported the idea of the low stored energy of the lambda fiber grains. A novel methodology has been developed for converting the nanoindentation load-displacement data into indentation stress-strain curves and extracting the elastic and post-elastic behavior. Extracted variations of effective indentation modulus with orientation were in excellent agreement with previously developed model. Furthermore, an intrinsic orientation dependence of indentation yield strength was extracted in a strain-free material. Developed nanoindentation methodology was successfully used for characterization of microstructure evolution in terms of stored energy variation with orientation during plane strain compression. Variations in stored energy at the grain-scale level were extracted from an increment in indentation yield due to increase in dislocation

density. It was found that nanoindentation yield strength is about 2 times the yield strength of homogeneous compression. Moreover, higher indentation yield strength was observed in regions that have rotated during deformation to non-lambda orientations with higher Taylor factors. Experimental results have supported idea of correlation between the Taylor factor and stored energy that was used in multistage processing for successful recovery of lambda texture. Hypothesis for observed much higher strain hardening in nanoindentation than in homogeneous plane strain compression is that the rate of generation of new dislocations is dependent on the dislocation density alone while the rate of annihilation of dislocation is strongly dependent on both dislocation density and the type of dislocations being generated which can be influenced by deformation mode.

CHAPTER 1: INTRODUCTION

Electrical steel is specialty steel known for its excellent soft magnetic properties achieved by high solute level of silicon [1]. High silicon content contributes to high electrical resistivity and low magnetic losses [2], which makes this alloy extremely attractive for electrical devices such as transformers, motors and generators. The material is usually manufactured by thermomechanical processing in thin strips, less than 2 mm thick, also called laminations.

Constant growth in electrical power consumption requires development of better steels for highly efficient electrical machines to decrease wasteful dissipation of energy which is converted into heat and has a negative impact on our environment.

The development of grain oriented electrical steel by Goss [3] has been a great scientific and technological achievement in controlling the texture and improving the magnetic properties of soft magnetic alloys. For transformer sheet application, the Goss {011}<100> readily produced and Cube {100}<001> produced only with difficulty textures provide superior magnetic properties since <100> direction is parallel to the rolling direction (RD) and transformers are designed in such a way that the magnetic field travels in a closed loop along rolling direction, i.e. <100> direction, which is the easy direction of magnetization [4, 5].

However, in AC motors and generators designed by Tesla [6], where the magnetic field constantly rotates in a plane, the Goss {011}<100> (very poor since it contains the <011> hard direction) or Cube {100}<001> (very difficult to produce in BCC alloys) annealing textures of rolled electrical steel are not adequate. The texture that should give the best magnetic properties is lambda fiber where the <001> crystal direction is normal

to the sheet, while the other two directions, <100> and <010>, are distributed uniformly in the plane of sheet (Figure 1). Goss textured sheet has been the industry standard for many years, while sheets with the lambda fiber have never been produced commercially in the iron-silicon steel.

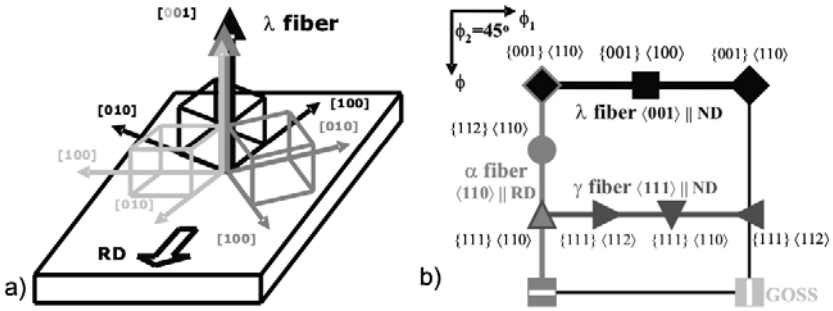

Figure 1: Schematic representation of: a) preferred lambda fiber texture for AC motors, b) ϕ_2=45° section of the Euler space with positions of lambda fiber, Goss component and the commonly developed alpha and gamma fibers on rolling in BCC iron.

The commercial processing of sheets with the preferred lambda fiber should be possible by twin roll casting described by Bessemer [7]. Twin roll casting technology is available for aluminum alloys [8] and steels [9]. Twin roll casting can produce thin sheets with a quite strong lambda fiber texture if the direction of solidification is normal to the sheet which it is expected in low conductivity iron alloys. Alternatively, directional solidification (DS) yields the desired <001> fiber texture. Sadly so far our Brazilian collaborators were unable to produce the desired grain structure in twin roll cast samples but were successful in producing it in a conventional DS experimental set up and columnar grained ingots of electrical steel are also routinely produced. These materials were the ones used in the present investigation. Further processing of this industrial cast material is however required to try to maximize the retention of the preferred lambda

fiber after the required rolling (needed to optimize the sheet thickness and grain size to about 150-200 microns [10, 11]) and annealing (needed to reduce the dislocation density) to give the best magnetic properties.

Alternatively, the lambda fiber can be produced by directional solidification [12], where during solidification the direction of dendritic growth in cubic metals (FCC as well as BCC) is <100> and the desired texture is conventionally produced in regions of columnar grain growth [13, 14].

Landgraf reported very low magnetic losses in the directionally solidified electrical steel with a columnar grain structure near the ideal lambda fiber texture [15]. Unfortunately, after applied additional heavy rolling and recrystallization in order to obtain sheets with optimal thickness and grain size for electric motors the preferred lambda fiber from the as-cast state was largely destroyed and the magnetic properties deteriorated [16].

Following discussion between Doherty and Landgraf in 2002 on the loss of the preferred lambda fiber texture, an additional processing step was proposed to try to restore the previously lost lambda fiber texture. The additional step was a light (≈10%) rolling reduction followed by recrystallization of the previously heavily rolled and recrystallized directionally solidified electrical steel. The proposed suggestion was successful and the additional processing step recovered much of the lost lambda fiber texture.

The hypothesis for the processing was (i) that grains close to the desired orientation were expected to have low stored energy (reflected by their low Taylor factors) after rolling [17, 18], and (ii) that, on recrystallization after light rolling, the

likely recrystallization mechanism would be Strain Induced Boundary Migration (SIBM) [19], that had been reported to operate in lightly rolled pure iron [20]. In the study by Inokuti and Doherty [20], grains with a gamma fiber orientation, {111} parallel to the rolling plane, known to have high stored energy [21, 22], were preferentially invaded by recrystallized grains. Typically, in heavily rolled BCC iron, alpha fiber with <110> parallel to the rolling direction and gamma fiber are developed [21, 22]. Therefore, for the proposed hypothesis to work, some of the lambda fiber grains will need to remain after the prior heavy rolling and deformation.

The present study was carried out to investigate and validate these working hypotheses using both experimental and modeling investigations. Samples of continuously cast single-phase polycrystalline columnar-grained electrical steel were subjected to rolling and annealing processes. Also, samples of directionally solidified single-phase polycrystalline columnar-grained electrical steel were subjected to a channel-die compression (the deformation process simulates rolling) at room temperature and subsequent annealing.

CHAPTER 2: BACKGROUND

Two of the most important and widely used processes in manufacturing of polycrystalline metallic alloys are plastic deformation and recrystallization. The microstructure changes during deformation in various ways and the most obvious is the shape change of the grains. Other features are the changes of internal structure within the grains. In addition, the initial orientation of single crystals or individual grains in the polycrystalline sample change during deformation. These changes are not random and contribute to heterogeneous deformed state of material with rotation of grains or their segments towards preferred orientations (textures). It is the deformed microstructure that controls the development of the microstructure and texture in the subsequently recrystallized material and associated properties.

2.1 Deformation

Heterogeneity of the deformed microstructure has been recognized for a long time and studied at various length scales from atomic to single crystals and polycrystals [18, 23-30]. Simultaneously with the characterization of deformed microstructure, study of deformation mechanism has evolved in order to explain processes behind the changes of microstructure and texture during deformation. Change in orientation and shape of individual grains in a polycrystalline material is caused by plastic flow due to generation of dislocations moving in certain directions (slip directions) within certain planes (slip planes). The progress of reorientation is gradual and leads to the development of texture or preferred orientation of the grains as well as a preferred shape change of the grains. Several crystal plasticity theories were developed [31, 32] to predict which slip systems (combination of slip direction and slip plane) are possible to operate and determine the

resulting texture. Sachs model [31] assumes that only the most stressed slips systems are operational, while Taylor model [32] assumes that all grains are subjected to the same strain. In the realm of these assumptions the Taylor model enjoyed great success.

Lately, immense progress has been made in implementation of crystal plasticity models in finite elements codes [32-36]. They were successful in predicting the average crystallographic texture, but failed in predicting the orientation of individual grains in the sample. In recent comparison of Taylor-type models, which assume homogeneous deformations within the individual grains, and the crystal plasticity finite element models, which allow non-homogeneous deformations inside the grains, with the carefully designed experiments, models failed [37, 38]. The main reason for the failure of the models in predicting the evolution of microstructure at the grain-scale level is that they do not adequately capture the underlying physics of grain fragmentation. Experimental studies have shown that each grain splits into a range of significantly different orientations [20, 38-42].

In the complex deformed microstructure grains are usually broken down into separate and misoriented fragments. The development of grain fragmentation is a consequence of crystallographic slip and it is inevitable when different parts of the grain rotate to different orientation by selection of different combination of slip systems during imposed deformation. Detailed deformation study of commercially pure aluminum with coarse columnar grains has shown two types of grain fragmentations, those with repeating orientation fields and those with non-repeating orientation fields [38]. Fragmentation of the grains with repeating orientation fields was explained as an inherent instability of initial crystal orientation when subjected to particular deformation mode.

On the other hand, fragmentation of the grains with non-repeating orientation fields was seen as a natural consequence of the grain interaction. This was particularly observed when a smaller and/or softer grain had a common boundary with the larger and/or harder grain. In the same study, the micro-mechanical finite element simulations using the crystal plasticity models did predict development of in-grain misorientations with an imposed deformation, but the extent and nature of these in-grain misorientations did not match the measured values.

As a consequence of grain fragmentation due to inhomogeneous deformation and change of grain shape due to change of sample shape the total grain boundary area in the material increases. Developed regions that accommodate the misorientation between adjacent fragmented regions that have rotated in different ways within the grain are named transition bands. At moderate strains transition bands have a finite width and can be distinguished from the prior grain boundaries. However, at higher strains transition bands collapse from finite width to atomically sharp boundaries and cannot be clearly distinguished from original high angle grain boundaries [42]. High angle boundaries have a high mobility and play an important role in dislocation rearrangements and formation of low dislocation density regions necessary for formation of recrystallization nuclei.

2.2 Recrystallization

During deformation most of the work expended is released as heat and a very small amount remains as stored energy in the metal. This stored energy arises from dislocations generated during plastic deformation. Generated dislocations and dislocation structures are the source of heterogeneity in deformed microstructure and associated difference in stored energy is the driving force for nucleation and growth of almost

dislocation free grains during subsequent annealing. Numerous studies of annealing phenomena have shown that nucleation and growth of recrystallized grains as well as the recrystallization texture strongly depend on the deformed state of previously cold worked metal [19, 40, 43-49].

Nucleation of new grains during recrystallization of the deformed metals is a heterogeneous process that occurs at particular features of the microstructure such as original grain boundaries, transition bands, precipitated particles and inclusions [50-54]. The classic example of recrystallization by grain boundary migration is that of moderately deformed high purity aluminum [19] and high purity iron [20, 39]. In both cases initiation of recrystallized grains was driven without the formation of new nuclei by so called Strain Induced Boundary Migration (SIBM) mechanism. On the other hand, numerous recrystallization studies [19, 40, 44, 47, 48, 54-56] have shown that the in-grain misorientations developed by grain fragmentation and formation of transition bands play a central role in the nucleation of new grains during recrystallization of more heavily deformed metals.

It is now well understood that the new recrystallized grains grow from small regions, recovered subgrains or cells, already present in the deformed microstructure [44, 45]. An important outcome of this concept is that the orientation of each recrystallized grain arrives from the same orientation present in the deformed microstructure [48, 51, 54, 55, 57]. The ability of the nucleated grain to grow further is determined primarily by the orientations of the adjacent regions in the microstructure. It is found [54, 55] that only highly misoriented boundaries from adjacent regions (typically more than 15 degrees) possess the necessary mobility for recrystallization.

Another important fact is that during the recrystallization process, growing new grains invade their neighboring deformed grains and replace the deformed matrix. The replacement of deformed grains by recrystallized grains of a different orientations leads to development of recrystallization texture which is related to but usually quite different from the deformation texture [58]. As a result, the development of microstructural features in the deformed state that are vital to understanding of recrystallization phenomena can usually only be studied statistically [42].

Orientation pinning can occur in heavily deformed metals with very strong deformation texture where new recrystallized grains with orientations that are mostly present in the deformation texture will have their growth inhibited by contact with deformed regions of same or similar orientations [42, 59-61]. It was demonstrated how this phenomenon accounted for the much stronger cube texture in warm rolled commercial purity aluminum than in the equivalently cold rolled material [59, 62]. In this process about 80% of the deformed sub-grains with the deformation texture orientations start to nucleate but their further growth is inhibited by the formation of the low angle boundaries on impact of the new grain with similar oriented bands of deformed metal. These small grains are frequently consumed by larger grains with minority orientations which growth is driven by interfacial energy. For orientation pinning to be significant the size of the recrystallized grains needs to be larger than the spacing of similarly oriented regions of the deformed metals.

2.3 Microstructure and Properties

Grain size in the final recrystallized microstructure is largely determined by the frequency of the new grains that nucleate first while the texture is determined by either

the orientation of the new grains that nucleate first (frequency advantage) or the orientation of the grains that grow faster (size advantage). The importance of controlling the grain size can be emphasized through very well established Hall-Petch relationship where the yield strength of material is inversely proportional to the square root of the grain size [63, 64]. Effect of grain structure on properties was studied extensively [54, 56, 65, 66] and it was recognized that not only grain size but grain shape, grain size distribution, residual cold work grains, grain orientation and orientation distributions play an important role in determining material properties.

Recrystallization plays a vital role in the manufacturing of metallic alloys and control of microstructure and texture during recrystallization is of great economic importance as well. Crystallographic texture in a recrystallized rolled sheet affects the strain distribution and plastic flow during forming which leads to plastic anisotropy that significantly impacts the formability.

Excellent examples of importance for highest quality control of material properties are: (i) decrease of the earing during deep drawing of aluminum for beverage cans - achieved by the strengthening of the low stored energy cube texture in rolled high stacking fault energy FCC metals [67], and (ii) high formability during pressing of low carbon steels for auto body sheets - achieved by the strengthening of the high stored energy gamma fiber which has high r-value (ratio of lateral to through thickness strains) [68, 69].

Development of low stored energy grains with cube texture in FCC metals and in moderately deformed BCC metals is caused by nucleation from large number of grains of dominant orientation (frequency advantage) rather than from the larger growth of

dominant grains (size advantage). It was observed that subgrains of low stored energy orientations were usually larger and less misoriented from the adjacent subgrains [42, 59]. Local size advantage and high misorientation across the boundary between the grains of low and high stored energy are essential conditions for nucleation and recrystallization is driven by the stored energy difference.

On the other hand, recrystallization of heavily rolled BCC metals strengthens the high stored energy gamma fiber at the expense of the somewhat lower stored energy alpha fiber. High stored energy gamma grains also nucleate from large number of grains of dominant orientation (frequency advantage) and the possible explanation is the distribution of stored energies in gamma grains which provide a large enough differences in subgrain sizes and misorientations across boundaries which are essential for nucleation [22, 70, 71].

The grain oriented electrical steel for transformer cores is another well known example of controlling the recrystallization texture. The important requirement for sheets used for transformer cores is easy magnetization. As previously mentioned, magnetization is easiest along <100> crystallographic direction and great care is taken during multi stage processing to develop a strong <100> preferred orientation parallel with a rolling direction (RD). This is achieved by controlled dissolution of the second phase particles that leads to abnormal grain growth of grains with the preferred Goss texture from the grain structure previously developed in the recrystallized sheet. The details of the multi stage processing are, however, well kept industrial secret [72].

In addition, final recrystallized microstructure in electrical steel plays an important role in energy loss, also called the core loss or iron loss in the electrical

devices. The loss of energy (that is adversely converted into heat) can be divided in two components: hysteresis loss and eddy current loss. Hysteresis loss is caused by the migration of magnetic domains (regions within the grain with the same alignment of atomic magnetic moments) in the material when subjected to an alternating magnetic field. The direction of alignment varies from domain to domain and regions separating domains are called domain walls. The optimum grain size for electrical steel used in alternating magnetic field of 50 Hz is about 150-200 microns. The optimum grain size is linked with the magnetic domains, i.e. below the optimum grain size hysteresis loss due to domain wall interaction dominates, while above the optimum grain size hysteresis loss is related to the requirement of high velocity of domain wall movement. It is also important to have low dislocation density and residual stresses in the processed material since their presence impede a motion of domain walls that have to abide by the field of 50 Hz. Eddy current loss is due to the electric current generated in the material. Generated eddy current creates magnetic fields opposed to the field induced by the magnetization. Eddy current is linked to the resistivity of material. It was found that resistivity can be effectively increased (eddy current reduced) by addition of Silicon, however, it is limited to few percent due to reduction of workability [1, 15, 73].

2.4 Experimental Techniques

The advances in understanding the structural changes associated with thermomechanical processing were mainly limited by the development of techniques for materials characterization. With the advent of transmission electron microscopy, the deformation structure and its evolution during annealing could be studied in more details [39, 50, 55, 74-78]. Other techniques [39-42, 55, 79, 80], have included coarse-scale

30μm Kossel diffraction, finer scale TEM techniques on the scale of a few microns, and backscattered Kikuchi diffraction (BKD) in SEM techniques with a higher resolution and covering much larger areas. In the sets of experiments [38, 81], an effort was made to extend the two-dimensional observations into three-dimensional microstructures by use of polycrystals with a columnar grain structure.

There are two other possible experimental methods for characterization of the deformed and recrystallized microstructures in 3D. The first is serial sectioning, made more accessible by the use of focused ion beam (FIB) in SEM [82, 83]. This technique inevitably destroys the carefully characterized microstructure, which is thus not available for further study, for example, an investigation as to how nucleation might develop at a particular misorientation. Furthermore, serial sectioning is very time consuming and is limited to small areas. The second approach involves the use of high intensity very short wavelength X-rays using synchrotron radiation [84, 85]. This approach is very promising because the grain structures can now be characterized completely in 3D, and their evolution can be followed either during continued deformation or annealing in real time. The only drawback to this approach is the expense and difficulty of the study. Presently, this method allows only a few grains to be studied under low strains for deformed microstructures and spatially limited studies of recrystallization growth in more heavily deformed samples. In the next few years, it is expected to extend this technique to larger length scales and higher strains.

2.5 Objective

The objective of the present study is to develop insight in development of deformed microstructure from which the recrystallized microstructure evolves. Therefore,

more complete understanding of recrystallization process requires elaborated understanding of the deformed state which can only be done by full characterization of the microstructure experimentally and subsequently by developing of predictive deformation models to predict both average properties and local heterogeneities.

The main aim of the present study was to investigate and develop a thermomechanical processing route for recovery of the preferred lambda fiber in iron-silicon electrical steel needed for superior magnetic properties in electric motor application.

Experimental and modeling investigations were carried out to validate the orientation dependence of stored energy and to verify that grains with the orientation close to the desired lambda fiber have low stored energy (reflected by their low Taylor factors) after rolling and that strengthening of the preferred lambda fiber on recrystallization after light rolling is achieved by the Strain Induced Boundary Migration (SIBM) mechanism.

In addition, a novel experimental investigation was carried out in order to fully characterize the evolution of heterogeneous deformed microstructure at the grain-scale level (in terms of local orientations and stored energies) during deformation in a channel die compression through several deformation stages and the influence of developed heterogeneities on the nucleation of new grains during subsequent annealing.

CHAPTER 3: EXPERIMENTAL METHODS

The majority of industrially used metals are made up of many crystals (grains), each of which has an ordered structure. These crystals all fit perfectly together to form a solid polycrystalline metal. Although the structure within each of these crystals is ordered they are not aligned with the internal structure of the neighboring grains. This creates a grain boundary, which is an interface between two crystals whose structures are not geometrically aligned. These crystals are said to have different orientations or three dimensional configurations relative to the sample reference frame (Figure 2a).

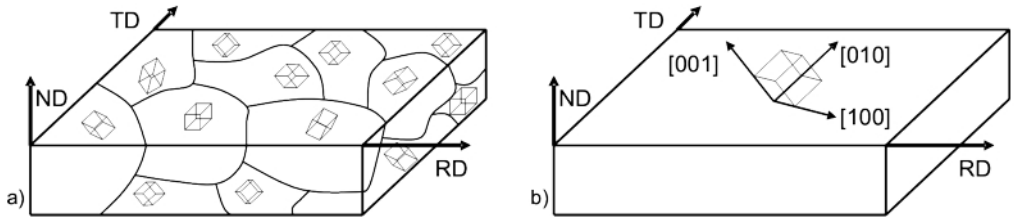

Figure 2: Schematic representation of: a) polycrystalline microstructure depicting the different orientation of the crystals, b) sample reference frame and crystal frame inside the bulk material.

In general, the crystallographic orientation of polycrystalline materials is not random, meaning that there is a preferred crystallographic orientation of the individual crystals or “crystallographic texture”. The significance of texture lies in the anisotropy of many macroscopic material properties (thermal expansion, electrical conductivity, elastic modulus, strength, ductility, toughness, magnetic permeability and energy of magnetization) [86]. In other words, the value of the property depends on the crystallographic direction. Therefore, the control of texture is of fundamental importance in materials processing as well as in material design.

3.1 Crystallographic Orientation

Orientation of individual crystals (grains) within a polycrystalline sample can be described as the rotation g, which transforms the fixed sample's coordinate system into fixed crystal's coordinate system [87]. Usually, sample's coordinate system is defined by rolling (RD), transverse (TD) and normal (ND) orthogonal directions and crystal's coordinate system is defined by Miller indices of cube direction [100], [010] and [001] which are also orthogonal (Figure 2b).

The orientation of a crystal relative to the sample reference frame can be represented by three rotations, also referred to as Euler angles (ϕ_1, ϕ, ϕ_2). There are multiple conventions for representing these rotations and the most commonly used is the Bunge convention [87]. The Bunge convention rotates the sample reference frame into the crystal frame and the rotation g is represented by the three Bunge-Euler angles. The three angles of rotation in the Bunge-Euler convention must be performed in the specific order relative to a specific axis of rotation to transform the sample axes to the crystal axes (Figure 3).

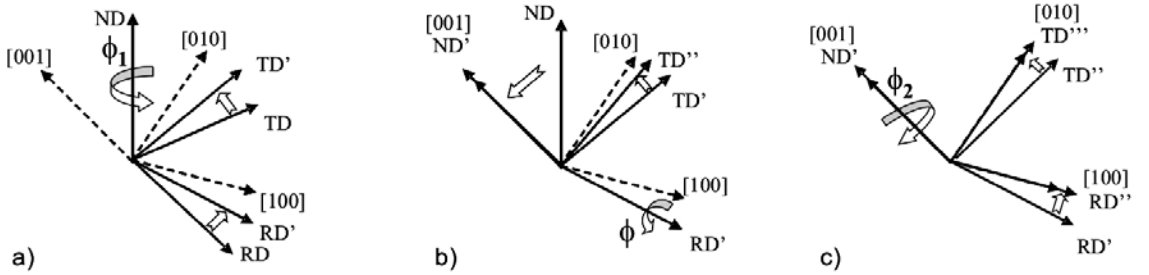

Figure 3: Schematic representation of the Bunge-Euler convention, which rotates the sample reference frame into the crystal reference frame.

Angle ϕ_1 is the first angle of rotation and is performed anticlockwise about the ND axis, ϕ is the second rotation and is performed anticlockwise about the RD' axis, and ϕ_2 is the final rotation and is performed anticlockwise about the ND' axis.

A complete description of texture can be expressed in terms of an orientation distribution function (ODF) plot in a three-dimensional orientation space, also called an Euler space [87]. In the Euler space orientations are plotted as a function of three Bunge-Euler angles, actually orientations are shown in sections as a function of two Bunge-Euler angles for a fixed value of a third angle. Typically, for BCC metals ϕ_1 and ϕ are varying from 0-90^o and ϕ_2 is fixed for section (0^o, 5^o, 10^o, … , 90^o). The ODF plot (Figure 4) is shown as a contour intensity plot and the regions of high intensity (near the dark end of the gray scale) are associated with the preferred orientation of the crystals. Lambda fiber texture is seen along ϕ_1 axis for ϕ equal 0^o in all ϕ_2 sections, this means that lambda fiber lies in the ϕ_1-ϕ_2 plane. Lambda fiber is also seen along ϕ_1 axis for ϕ equal 90^o in ϕ_2=0^o and its intensity decreases in ϕ_2=5, 10 and 15^o sections then disappears and appears again with the increasing intensity in ϕ_2=75, 80, 85 and 90^o sections. Actually ϕ_2=0 and 90^o are exactly the same due to cubic crystal symmetry of the BCC steel. For BCC metals it is common to plot only the ϕ_2=45^o section where other textures developed during rolling are seen as well (Figure 1).

In the first part of the study Orientation Imaging Microscopy (OIM) technique was used to investigate microstructure and texture evolution during thermomechanical processing of iron-silicon electrical steel.

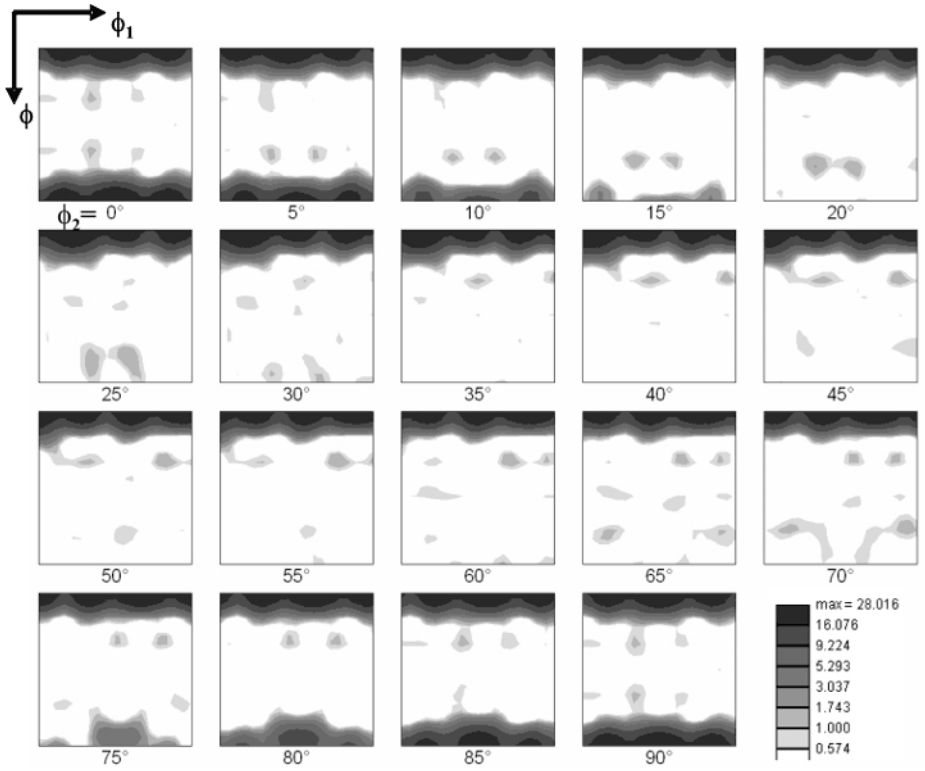

Figure 4: ODF of directionally solidified electrical steel with the lambda fiber texture.

3.2 Orientation Imaging Microscopy

Orientation Imaging Microscopy provides a link between the texture and microstructure and is a powerful technique for analyzing texture and grain boundary structure at the grain-scale level of polycrystalline materials. Orientation Imaging Microscopy technique is based on automatic indexing of electron backscatter diffraction (EBSD) patterns which can be accomplished in the scanning electron microscope (SEM) based system. Rapid capturing of large number of data makes the technique extremely attractive in texture studies [88, 89].

Electron backscatter diffraction (EBSD) patterns are obtained by focusing the electron beam on a crystalline sample (Figure 5a). The sample is tilted to approximately 70 degrees with respect to the horizontal which allows more electrons to be diffracted and

to escape towards the detector. The electrons disperse beneath the surface, subsequently diffracting among the crystallographic planes. The diffracted electrons produces a pattern composed of intersecting bands, termed electron backscatter diffraction (EBSD) patterns, or Kikuchi lines (Figure 5b). The patterns are imaged by placing a phosphor screen close to the sample in the SEM chamber.

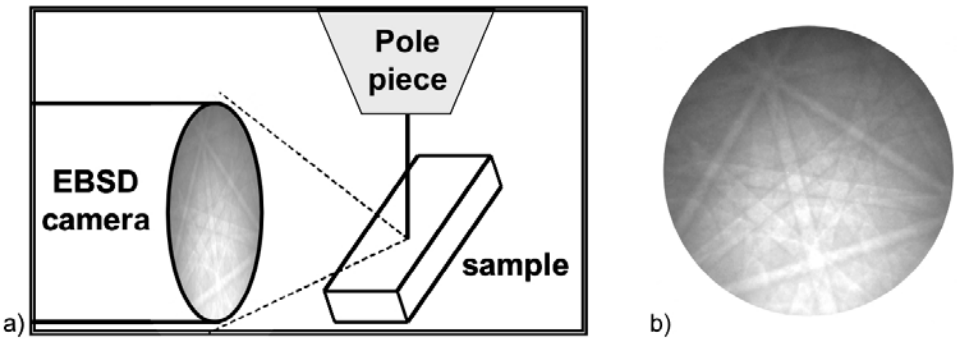

Figure 5: a) schematic of the sample inside the SEM chamber, b) EBSD pattern.

The bands in the pattern represent the reflecting planes in the diffracting crystal volume. Thus, the geometrical arrangement of the bands is a function of the orientation of the diffraction crystal lattice. The width and the intensity of the bands are directly related to the spacing of atoms in the crystallographic plane and the angles between the bands are directly related to the angles between the crystallographic planes. This technique allows crystal orientation information to be determined at very specific points in a sample. The spatial resolution varies with the accelerating voltage, beam current and spot size of the SEM along with the atomic number of the sample material. Indexable patterns can be obtained from about 0.05 microns with a field emission source.

In this study, texture measurements were obtained by using the TSL's OIM system fully integrated with the ESEM Philips XL 30.

3.3 Stored Energy

When metal is stressed beyond its elastic range, permanent changes occur in its structure and physical properties. Several types of structural defects are created in the deformed material, of which the most important for the mechanical properties and the recrystallization behavior are dislocations. As the deformation proceeds, the density of dislocations in the structure increases which is directly proportional to the stored energy of a plastic work [90]. With the increase of the dislocation density in the deformed structure the movement of the dislocations is impeded by the interactions with other dislocations. The dislocation density is a measure of how many dislocations are present in a material and is defined as the total length of dislocations per unit volume [m/m^3] or as the number of dislocation lines intersecting a unit area [$\#/m^2$].

In lightly deformed materials the dislocation density may be measured directly by transmission electron microscopy. On the other hand, in even moderately deformed metals the dislocation density is such high that it cannot be determined accurately. However, it is possible to obtain an estimate of the dislocation density from the mechanical properties of material. For example, the flow stress τ (the stress required to cause plastic deformation) of the material can be expressed as follows:

$$\tau \approx \alpha G b \rho^{\frac{1}{2}}, \tag{3.1}$$

where α has value between 0.5-1 depending on the dislocation arrangements, G is the shear modulus, b is the Burgers vector and ρ is the dislocation density.

Stored energy of deformation due to an increase in dislocation density can be expressed as follows:

$$E_s = \rho E_l, \tag{3.2}$$

where E_l is the energy per unit length of dislocation and has approximate value of Gb^2. Using the approximate value for the energy per unit length E_l and expressing the dislocation density ρ from the Eq. (3.1) and substituting in the Eq. (3.2) the stored energy is as following:

$$E_s = \frac{\tau^2}{\alpha^2 G}, \tag{3.3}$$

In addition, the stored energy of deformation (increase of the dislocation density) contributes to the work hardening of material. The work hardening can be defined as the increase in yield strength with increase in strain ($d\tau/d\gamma>0$, where τ and γ represents the flow stress and shear strain, respectively). Typically, there are three stages of strain hardening. Stage one of strain hardening is only seen for single crystals where dislocations glide to the surface on a single slip system (dislocation density remains constant). Stage two of strain hardening is seen for both single crystals and polycrystals when rapid trapping of dislocation occurs due to activation of multiple slip systems and it is empirically found that $d\tau/d\gamma \approx G/200$ increases linearly. Neglecting the factor α in Eq. (3.1) and finding a derivative the following is obtained:

$$\frac{d\tau}{d\rho} = 0.5Gb\rho^{-\frac{1}{2}}, \tag{3.4}$$

The intrinsic linear strain hardening due to continuous generation and trapping of dislocations with the increasing strain can be expressed as a power law relationship:

$$\frac{d\rho}{d\gamma} = \eta\rho^{\kappa}, \tag{3.5}$$

which can be further expressed as following:

$$\eta\rho^{\kappa} = \frac{d\rho}{d\gamma} = \frac{d\rho}{d\tau}\frac{d\tau}{d\gamma}, \tag{3.5}$$

Expressing $d\rho/d\tau$ from the Eq. (3.4) and substituting $d\tau/d\gamma$ with G/200 (the standard work hardening rate in stage two deformation [91]) in the Eq. (3.5) the following is obtained:

$$\eta\rho^{\kappa} = \frac{d\rho}{d\gamma} = \frac{d\rho}{d\tau}\frac{d\tau}{d\gamma} = \frac{2\rho^{\frac{1}{2}}}{Gb}\frac{G}{200}, \tag{3.6}$$

which gives $\eta=1/100b$ and $\kappa=1/2$. Finally, the intrinsic linear strain hardening due to continuous generation and trapping of dislocations by slip in stage two is as follows:

$$\frac{d\rho}{d\gamma} \approx \frac{\rho^{\frac{1}{2}}}{100b}, \tag{3.7}$$

Furthermore, Taylor factor is another parameter frequently used for indication of slip activity for imposed deformation and can be expressed as following:

$$M = \frac{\Sigma\Delta\gamma}{\Delta\varepsilon}, \tag{3.8}$$

where $\Sigma\Delta\gamma$ is the sum of the shears on the various slip planes and $\Delta\varepsilon$ is the normal strain imposed. Combining Eq. (3.7) and Eq. (3.8) for small increments of plastic strain the following relationship is obtained:

$$\Sigma\Delta\rho = \frac{\rho^{\frac{1}{2}} M\Delta\varepsilon}{100b}, \tag{3.9}$$

Eq. (3.9) was derived in collaboration with Doherty as an expected correlation between the stored energy (dislocation density) and the Taylor factor, i.e. for the given increment of imposed plastic strain the increment in stored energy is directly proportional to both created new dislocation and Taylor factor. The formulated link between the Taylor factor and stored energy supports the hypothesis that low Taylor factor values are associated

with low stored energy and vice versa. As mentioned in the Chapter 1 this was a central idea for recovery of the previously lost preferred lambda fiber during recrystallization by strain induced boundary migration mechanism after light rolling.

For the stage two of strain hardening it is assumed that all dislocations are generated by slip alone and that dynamic recovery of dislocations does not occur. The stage three of strain hardening begins when the linear strain hardening breaks down. This is caused by the fall in dislocation density due to destruction of dislocations by cross slip (dynamic recovery). With the further increase of the strain new dislocations are stored (ρ^+) but simultaneously dislocations get partially cancelled out (ρ^-) and the balance of retained dislocations can be expressed as following:

$$\frac{d\rho}{d\gamma} = \frac{d\rho^+}{d\gamma} - \frac{d\rho^-}{d\gamma}. \qquad (3.10)$$

where with the increasing strain and dislocation density the second term increases more than the first term and leads to the decrease of the strain hardening in the stage three. Possible explanation is that the rate of generation of new dislocations $d\rho^+$ is dependent on the dislocation density ρ alone (i.e. $d\rho^+/d\gamma=f(\rho)$) while the rate of annihilation of dislocation $d\rho^-$ is strongly dependent on both dislocation density ρ and the type of dislocations being generated $\Sigma\Delta\gamma$ (number of slip directions and Burgers vectors) in the microstructure (i.e. $d\rho^-/d\gamma=f(\rho,\Sigma\Delta\gamma)$) [92].

3.4 Nanoindentation

In the second part of the study orientation imaging microscopy was combined with the nanoindentation technique in order to test hypothesis that proposes orientation

dependence of the accumulated stored energy in the deformed polycrystals. It remains to be established to what extent is dynamic recovery ($d\bar{\rho}/d\gamma$) orientation dependent.

Nanoindentation technique involves pressing of an indenter with the known tip geometry on the flat surface of the sample. During indentation the load-displacement data is documented (figure 6a) from which useful information about the local mechanical properties can be extracted [93-95]. Nanoindentation is commonly used to measure the elastic modulus and the hardness of the material [96-98]. It has also been used for evaluating plastic response of material [99, 100].

Analysis of nanoindentation data is based on Hertz's theory [101] where the frictionless contact between two linear isotropic elastic solids with spherical surfaces can be described as follows:

$$P = \frac{4}{3} E_{eff} R_{eff}^{\frac{1}{2}} h_e^{\frac{3}{2}}, \qquad a = \sqrt{R_{eff} h_e}, \tag{3.11}$$

where P is the indentation load, h_e is the elastic penetration depth and a is the radius of the contact boundary between the indenter and the sample. E_{eff} and R_{eff} represent the effective Young's modulus and the radius of the indenter and the specimen, described as follows:

$$\frac{1}{E_{eff}} = \frac{1-\nu_s^2}{E_s} + \frac{1-\nu_i^2}{E_i}, \qquad \frac{1}{R_{eff}} = \frac{1}{R_i} + \frac{1}{R_s}, \tag{3.12}$$

where E and ν refer to the Young's modulus and the Poisson's ratio, while subscripts s and i refer to the specimen and the indenter, respectively. For elastic loading of a flat sample, R_s approaches infinity and $R_{eff}=R_i$. However, beyond the elastic limit the sample experiences significant plastic strains during loading and the subsequent unloading is not

from a flat surface anymore. It is recognized that the contact between the indenter and the sample in the unloading segment is strongly influenced by the geometry of the residual indentation that is left in the sample [97, 98]. On the other hand, highly accurate measurement of parameters R_s and a is extremely difficult.

Applying Oliver and Pharr method [97, 98], the Young's modulus can be estimated from the unloading part of the load-displacement data as follows:

$$E_{eff} = \frac{\sqrt{\pi}}{2}\frac{S}{\sqrt{A}} = \frac{S}{2a}, \qquad h_e = \frac{3}{2}\frac{P}{S}, \tag{3.13}$$

where S represents the slope of the unloading curve dP/dh_e (also known as harmonic stiffness in Continuous Stiffness Measurements (CSM) method of nanoindentation measurements) and A represents the projected contact area (πa^2) between the indenter and the sample. In CSM technique, simultaneously with forcing the indenter tip into the surface an oscillating force with the force amplitude several orders of magnitude smaller than the nominal load is applied. This method provides measurements of contact stiffness at any point along the loading curve and not only at the point of unloading as in the conventional measurements [102].

Field and Swain [103] have originally proposed using the indentation stress-strain curves to characterize the local stress-strain behavior of a material. Indentation stress and indentation strain can be defined by rearranging Eq. (3.11) such that:

$$\sigma_{ind} = \frac{P}{\pi a^2}, \qquad \varepsilon_{ind} = \frac{a}{R_{eff}}, \tag{3.14}$$

The above described indentation strain has a weakness because, as mentioned earlier, $R_{eff}=R_i$ is true only for initial elastic loading and this approximation breaks down once

the sample experiences any significant larger plastic strains. In addition, the fundamental definition of the strain is the ratio of change in length over the initial length.

Recently, a new approach for extracting the indentation stress-strain curves has been developed at Drexel by Kalidindi and Pathak [104] where a new definition of the indentation strain was formulated by rearranging Eq. (3.11) differently such that:

$$\sigma_{ind} = \frac{P}{\pi a^2}, \qquad \varepsilon_{ind} = \frac{4}{3\pi}\frac{h_e}{a} \approx \frac{h_e}{2.4a}, \tag{3.15}$$

This form of definition of the indentation strain and the previously mentioned fundamental definition of the strain suggest use of the total indentation depth h_t (figure 6b) instead of the elastic indentation depth h_e:

$$\varepsilon_{ind} = \frac{4}{3\pi}\frac{h_t}{a} \approx \frac{h_t}{2.4a}. \tag{3.16}$$

This definition of the indentation strain allows distinguishing elastic and post-elastic behavior of material during indentation. It is also in accord with the defined primary zone of deformation during indentation (Figure 6b), where a cylindrical region of radius a and height of 2.4a is compressed by h_t. This provides a more physically valid description.

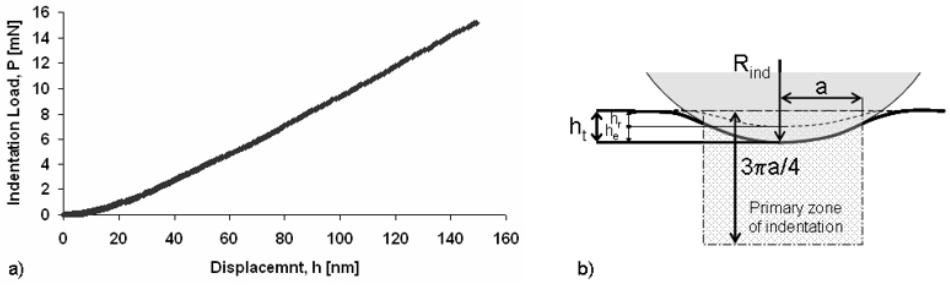

Figure 6: a) Example of load-displacement curve for electrical steel, b) sketch of the primary zone of indentation for spherical indentation.

CHAPTER 4: MODELING METHODS

Extensive prior research has provided substantial evidence for variations of stored energy in the deformed structure with the crystallographic orientation [17, 18, 22, 41, 42]. Since stored energy is driving force for recrystallization it is of great interest not only to correlate but also to quantify these values. The previously mentioned concept of Taylor factor (Eq. (3.8)) is very useful in quantifying the stored energy (increase in dislocation density).

4.1 Taylor Factor

The Taylor factor is a scalar value that provides an indication of the macroscale resistance to plastic deformation in terms of the slip resistance at the individual slip system. Therefore it is a strong function of the microstructure, i.e. the crystal orientations present in the sample. It can also be defined for individual crystals for a selected deformation mode.

The macroscopic power done per unit volume ω can be expressed as follows:

$$\omega = \bar{\sigma} \cdot \dot{\bar{\varepsilon}}^{p}, \tag{4.1}$$

where $\bar{\sigma}$ is the macroscopic equivalent stress and $\dot{\bar{\varepsilon}}^{p}$ is the macroscopic equivalent plastic strain rate and the index p is to denote plasticity. This relationship is valid only for small strains. However for large strains, the velocity gradient tensor $\mathbf{L^p}$ is used instead of $\dot{\bar{\varepsilon}}^{p}$. The velocity gradient tensor is expressed by the following relationship:

$$\mathbf{L^p} = \dot{\gamma}^{\alpha} \mathbf{m^{\alpha}} \otimes \mathbf{n^{\alpha}}, \tag{4.2}$$

where $\dot{\gamma}^{\alpha}$ is the shear strain rate in the slip system α and $\mathbf{n^{\alpha}}$ and $\mathbf{m^{\alpha}}$ represent the slip plane normal and a slip direction in the slip system α, respectively. When slip occurs on

multiple slip systems the velocity gradient tensor is used to sum over all active slip systems:

$$\mathbf{L^p} = \sum_{\alpha} \dot{\gamma}^{\alpha} \mathbf{m}^{\alpha} \otimes \mathbf{n}^{\alpha}, \tag{4.3}$$

For large strains the Eq. (4.1) can be written as follows:

$$\omega = \overline{\sigma} \cdot \mathbf{L^p} = \overline{\sigma} \cdot \mathbf{D^p}, \tag{4.4}$$

where $\mathbf{D^p}$ is a symmetric part of velocity gradient tensor. The elastic component is insignificant compared to the plastic component so it can be ignored. The velocity gradient tensor can also be decomposed as $\mathbf{L^p=D^p+W^p}$, where $\mathbf{W^p}$ is the anti-symmetric part of velocity gradient tensor. The symmetric component $\mathbf{D^p}$ can be written as follows:

$$\mathbf{D^p} = \sum_{\alpha} \frac{\dot{\gamma}^{\alpha}}{2} (\mathbf{m}^{\alpha} \otimes \mathbf{n}^{\alpha} + \mathbf{n}^{\alpha} \otimes \mathbf{m}^{\alpha}), \tag{4.5}$$

Microscopic power imposed on the material is expended by slip in the grains on all active slip systems in the material and it can be written as the following:

$$\omega = \sum_{\alpha} \tau_{\mathrm{CRSS}}^{\alpha} \dot{\gamma}^{\alpha}, \tag{4.6}$$

where $\tau_{\mathrm{CRSS}}^{\alpha}$ is the critical resolved shear stress for the slip system α.

The macroscopic and microscopic powers have to be equal, therefore:

$$\overline{\sigma} \cdot \dot{\bar{\varepsilon}}^{\mathrm{p}} = \tau_{\mathrm{CRSS}}^{\alpha} \sum_{\alpha} \dot{\gamma}^{\alpha}, \tag{4.7}$$

and Taylor factor **M** is defined as:

$$\mathrm{M} = \frac{\overline{\sigma}}{\tau_{\mathrm{CRSS}}^{\alpha}} = \frac{\sum_{\alpha} \dot{\gamma}^{\alpha}}{\dot{\bar{\varepsilon}}^{\mathrm{p}}}, \tag{4.8}$$

Five independent equations exist in Eq. (4.5) for the symmetric part of the velocity gradient tensor. This is because it is symmetric and the slip tensor ($\mathbf{m}^{\alpha}\otimes\mathbf{n}^{\alpha}$) is traceless, that is $\mathbf{m}^{\alpha}\bullet\mathbf{n}^{\alpha}=0$. Using the equation for the velocity gradient tensor, the shear strain rate can only be solved for if five independent slip systems can be selected from all possible slip systems. For a slip system to be independent it must not be able to be expressed by a combination of the other four slip systems. However, the solution obtained by solving Eq. (4.5) for five independent slip systems will not be unique. The uniqueness problem can be addressed by the rate dependent, visco-plastic model where a power law has been used to describe the rate-dependence of slip as following:

$$\dot{\gamma}^{\alpha}=\dot{\gamma}_{o}\left(\frac{\left|\boldsymbol{\sigma}'\cdot\frac{1}{2}(\mathbf{m}^{\alpha}\otimes\mathbf{n}^{\alpha}+\mathbf{n}^{\alpha}\otimes\mathbf{m}^{\alpha})\right|}{s^{\alpha}}\right)^{\frac{1}{m}}\operatorname{sgn}\left(\frac{\boldsymbol{\sigma}'(\mathbf{m}^{\alpha}\otimes\mathbf{n}^{\alpha}+\mathbf{n}^{\alpha}\otimes\mathbf{m}^{\alpha})}{2}\right). \qquad (4.9)$$

where $\boldsymbol{\sigma}'$ is the deviatoric stress tensor (stress can be decomposed into a hydrostatic part $\boldsymbol{\sigma}_{\mathbf{m}}$ and a deviatoric part $\boldsymbol{\sigma}'$, that is: $\boldsymbol{\sigma}=\boldsymbol{\sigma}_{\mathbf{m}}+\boldsymbol{\sigma}'$) and $\dot{\gamma}_{0}^{\alpha}$, m and s^{α} are material parameters representing the reference shear rate, rate sensitivity, and the slip system deformation resistance, respectively. Using equation (4.9) and replacing $\dot{\gamma}^{\alpha}$ in the Eq. (4.5) for symmetric part of velocity gradient tensor ($\mathbf{D}^{\mathbf{p}}$), the five equations with five unknowns of $\boldsymbol{\sigma}'$ components are obtained which provide unique solution.

The crystal plasticity modeling accounts for the physics of plastic deformation in a crystalline region at the microscale level and predict the response of a polycrystalline sample at the macroscale level. Several successful models have been developed for predicting the behavior of crystals during plastic deformation, namely the Taylor model [32] and micromechanical finite element model [33].

4.2 Taylor Model

The well know approach to obtain the response of a polycrystal from the response of the individual grains is to use Taylor's assumption. In Taylor analysis it is assumed that each individual grain undergoes the same shape change as the macroscopic body being deformed. In other words, all grains experience the same (uniform) deformation. The second assumption is that all grains have an equal volume. This implies that the stress in the polycrystal can be calculated as an average stress from all grains.

4.3 Finite Element Model

In this approach, the micromechanical finite element model is used to make the transition from the response of individual grains and predict the response of a polycrystalline sample. Each grain is modeled by one or more finite elements to allow for non-uniform deformation within the grains and between the grains. While Taylor model satisfies strain compatibility only, the micromechanical finite element model satisfy both, strain compatibility and stress equilibrium.

In this study, Taylor model and micromechanical finite element model were used to investigate the orientation dependence of Taylor Factor (M) values that has been previously reported [17, 18]. Furthermore, both models were also used to predict the texture evolution during deformation and the results were compared with the experimental data.

CHAPTER 5: EXPERIMENTAL RESULTS

5.1 Materials

Original plan was to obtain twin roll cast electrical steel from our collaborators at the University of Sao Paulo (USP), however, due to lack of the needed industrial scale resources they were unable to make twin roll cast Fe-Si with the required columnar microstructure. Two other types of material were provided instead and used in this study, namely DS Fe-Si ingot and commercial Fe-Si-Al ingot, both with columnar structure.

For studying the texture evolution during deformation and recrystallization and developing a processing route that recovers the desired <001> fiber, samples for rolling were cut out from a 50x50x50 mm block of a commercial ingot of continuously cast iron-silicon-aluminum alloy which had columnar grain structure. Samples were cut by electric discharge machining (EDM) in such a way that columnar grains have the <001> direction parallel to the normal direction (ND) (Figure 7). In this way, the sample has the <001> fiber parallel to ND, which matches the texture in directionally solidified material, previously investigated [16]. The dimensions of the cut samples were: 49x9.5x6.2 mm.

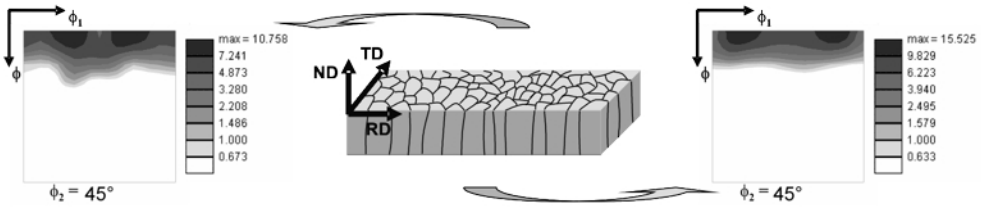

Figure 7: Schematic of the prepared sample with the ODF plots showing lambda fiber at the top and bottom sides in the continuously cast iron-silicon alloy.

The orientations of the columnar grains were determined by scanning the top and bottom surfaces of the sample. Having columnar grains that run through the thickness of

the sample and characterizing the two opposite sides provides a nearly complete characterization of the three-dimensional microstructure. The as-cast sample had a very large grain size of about 3mm, measured on a plane normal to the columnar growth direction and the orientation data was collected from 40 grains on both top and bottom sides. OIM data show that all the as-cast grains had <001> within 15^{o} of ND (Figure 8).

Samples for OIM study were prepared by mechanical grinding and polishing of both the rolling plane surface and the midplane section using a Struers grinding and polishing machine. After grinding by Si-C papers, 3 and 1 micron diamond suspensions were used for polishing in combination with several etches by Nital (5% volume mixture of nitric acid in ethanol). Final polishing was done by 0.05 micron colloidal silica.

Samples of directionally solidified iron-silicon alloy with a columnar grain structure were used for studying the microstructure evolution during deformation in a channel die and the influence of developed heterogeneities on the nucleation of new grains during subsequent annealing. In addition, the measured initial orientations were also used in a finite element simulation of a channel die experiment. Samples with the dimensions: 9x9x15 mm (Length x Width x Height) were also cut by EDM such that columnar grains have the <001> direction parallel by compression direction (Figure 8).

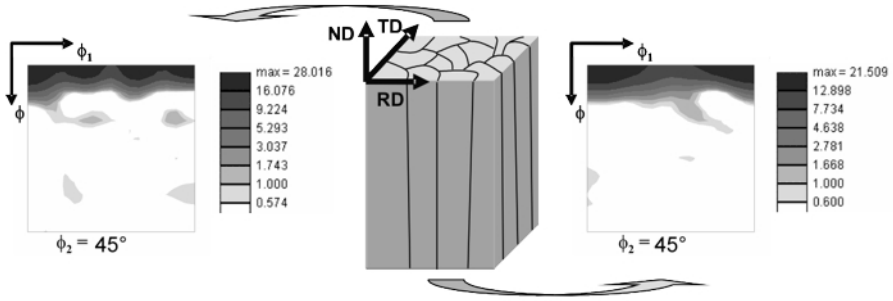

Figure 8: Schematic of the prepared sample with the ODF plots showing lambda fiber at the top and bottom sides in the directionally solidified iron-silicon alloy.

OIM measurements from 20 grains on top and bottom sides show that all the as-cast structure had <001> within 11^{o} from the compression direction (Figure 8). The directionally solidified material also had very large columnar grains of diameters of about 3mm and heights spanning the sample. The in-grain misorientation in the directionally solidified material was around 1^{o}. This value is lower compared to 6^{o} previously reported for directionally solidified high purity aluminum [81].

Samples for OIM and nanoindentation study were prepared by mechanical grinding and polishing using a Buehler grinding and polishing machine following the same procedure as described above. Furthermore, to minimize roughness and deformed layer developed during previous preparation steps, the final step included vibratory polishing by 0.02 micron colloidal silica using a Buehler vibratory polisher for a several days. The chemical compositions of the single phase Fe-Si alloys are given in Table 1.

Table 1: Chemical composition of the as-cast alloys (wt. %).

Casting	Fe	Si	Al*	C	S	N	O
Cont. cast.	Balance	3.2 %	0.96 %	34 ppm	9 ppm	18 ppm	17 ppm
Direct. Sol.	Balance	3.0 %		0.026 %	8 ppm	16 ppm	35 ppm

* Aluminum had been added to increase the electrical resistivity and thus decrease eddy current losses.

5.2 Rolling Experiment

5.2.1 Thermomechanical Processing

The continuously cast electrical steel was rolled on a Stanat laboratory rolling mill with 150 mm diameter rolls. In initial studies, the aluminum alloyed coarse grained columnar steel cracked badly on rolling at room temperature. Even, after initial preheating at 350^{o}C for 1 hour before the first rolling pass, severe cracking occurred

during the second rolling pass. However, after preheating for 1 hour at 350^{o}C before the first rolling pass and before each subsequent rolling pass at the same temperature for 15 minutes, only limited cracking occurred along edges. 350^{o}C was warm enough to avoid cracking during deformation but cold enough to prevent any significant recrystallization during successive reheating. The sample was rolled to thickness of 0.75mm (90% reduction) in 27 light reductions, giving a von Mises equivalent strain of 2.44.

After heavy rolling, part of the sample was retained for texture analysis and the rest of the sample was recrystallized at 800^{o}C/1h. Again a part of the sample was retained for structural analysis and the remaining material again rolled, but this time at room temperature with a light rolling reduction to the von Mises equivalent strain of 0.12 (10% reduction). At this time, the sample thickness was 0.7mm. Again a part was retained and the remaining material was recrystallized at 760^{o}C/1h. Subsequently, the second light rolling reduction with the same strain followed by recrystallization at 760^{o}C/1h was repeated again.

The idea for the third step was that if the proposed model for lambda fiber recovery by SIBM of the low Taylor factor of the <100> grains was correct, then due to the increased frequency of the lambda fiber grains, after the *first* application of the light deformation process, a *second* application should further strengthen the texture due to the increased number of lambda fiber grains to act as nucleation sites. As noted above, after each processing step, a piece of the sample was retained and its texture measured by the OIM. Friction between rolling mills and sample lead to a different stress state at the surface and midplane, therefore, the texture was measured at both the surface and at the midplane of the sample after each recrystallization step of the three stage processing.

From the inverse pole figure (IPF) maps (Figure 9) of the microstructures from ND sections obtained from both near the surface and at the midplane for the recrystallized samples it can be seen that, on recrystallization after the 90% reduction, only a few grains remain close to the lambda fiber (colored red). However, there is a recovery of the lambda fiber components on recrystallization after the first light reduction and this increased markedly, especially at the midplane, after the final processing step.

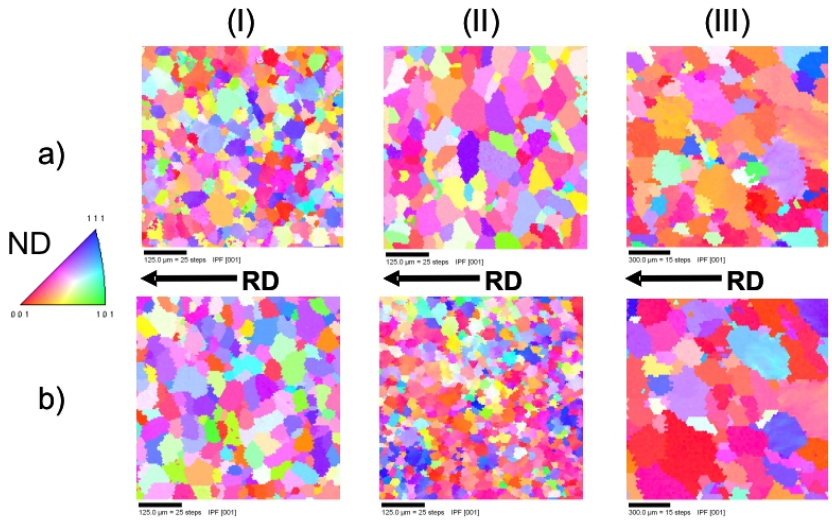

Figure 9: ND IPF maps of the recrystallized structures at a) surface and b) midplane after (I) the 90% reduction, (II) the first 10% reduction and (III) the second 10% reduction.

The recrystallized grain sizes are much smaller than the initial size, however, the grain size increased noticeably after the final processing step. The area weighted grain size averages are given in Table 2. The significant decrease in the grain size between the as-cast structure and that after heavy deformation followed by recrystallization indicates that almost all of the recrystallized grains were nucleated within the prior grains. That is, they arose from misorientations developed within the prior grains during the heavy

rolling. Only with local misorientations greater than about 15° can new grain nucleate during recrystallization [48, 54].

Table 2: Grain sizes of as-cast structure and recrystallized structures after deformation and mean Taylor factor (M) for recrystallized structures.

	As-cast	90% reduction	1st 10% reduction	2nd 10% reduction
Surface	3 [mm]	50 [μm]	80 [μm]	250 [μm]
Midplane	3 [mm]	90 [μm]	40 [μm]	230 [μm]
Mean Taylor factor	2.3	3.2	2.9	2.7

From the orientation distribution function (ODF) plots (Figure 10) for the ϕ_2=45° section and analyzing both near the surface and at the midplane it can be seen that after the 90% reduction only two components of initial lambda fiber remained in both surface and midplane, namely $\{001\}<3\bar{8}0>$ and $\{001\}<\bar{3}\bar{8}0>$.

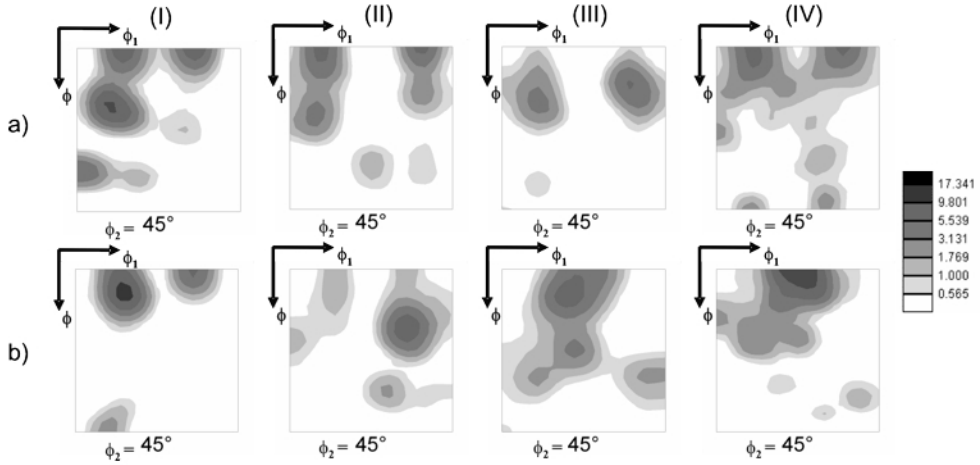

Figure 10: ODF plots from a) surface and b) midplane after (I) the 90% reduction and after subsequent recrystallizations following (II) the 90% reduction, (III) the first 10% reduction, (IV) the second 10% reduction.

At the surface (Figure 10-Ia), a large orientation spread from the lambda fiber towards gamma fiber occurred while at the midplane (Figure 10-Ib) a near $\{112\}<5\bar{9}2>$ component formed. This is only 12^{o} away from lambda fiber. In the previously investigated directionally solidified material rotated cube, {001}<110>, was found after heavy deformation [16]. However, after recrystallization at the surface (Figure 10-IIa) the orientations remained spread between the lambda and gamma fibers and at the midplane (Figure 10-IIb) strengthening of near $\{449\}<\bar{2}\bar{7}4>$ occurred. These results are similar to those reported in the previous study on laboratory directionally solidified Fe-3%Si [16].

With the *first* 10% reduction the as-rolled textures, surface and midplane, changed little, and after recrystallization (Figure 10-IIIa) the surface had even less components near the lambda fiber. The surface orientations seen after the first recrystallization that were well away from the lambda fiber have however vanished after this second recrystallization. At the midplane (Figure 10-IIIb), however, a strong texture components near the lambda fiber component centered on $\{115\}<\bar{1}\bar{6}1>$, that is only 16^{o} from the lambda fiber, was found. There is also some intensity at the perfect cube orientation $\{001\}<0\bar{1}0>$. The strengthening of the near lambda fiber, after a light rolling reduction, is also similar to that reported in the previous study on laboratory directionally solidified Fe-3%Si [16]. After the *second* 10% reduction again the textures changed little but after the final recrystallization, the lambda fiber components at the surface (Figure 10-IVa) and especially at the midplane (Figure 10-IVb) were, as predicted by the working hypothesis, found to be significantly strengthened by this final stage of processing. After the final processing step, at the surface, there are two lambda fiber components, $\{001\}<4\bar{9}0>$ and $\{001\}<\bar{4}\bar{9}0>$. At the mid-plane, there is one very strong lambda

fiber component near the cube orientation, <100>{001} with a maximum intensity. The combination of these two textures should give an approximately uniform lambda fiber through the thickness.

Therefore, as a result of the *two* successive light rolling reduction and recrystallization steps, the desired texture in the sample has been largely recovered and should have excellent magnetic properties for electric motor applications. Unfortunately the residual edge cracking in the sample prevented a valid evaluation of the magnetic properties. However despite the cracking, the sample showed satisfactorily low magnetic losses. It should be noted that the Al free directionally solidified Fe-3%Si steel has been channel die compressed to 80% reduction at room temperature with no cracking. Channel die compression of the Aluminum containing steel cracked after 40% reduction again at room temperature.

5.2.2 Crystal Plasticity Modeling

Crystal plasticity models were used to test the hypothesis that the lambda fiber grains (<001> normal to the rolled sheet) have low stored energies or at least the low Taylor factors associated with the low stored energy. As previously described, the Taylor factor is defined as the ratio of the sum of the shears on the various slip planes $\Sigma d\gamma$ to the total normal strain imposed $d\varepsilon$, in this case by rolling. The simulations were done using both the simple Taylor model [32], and also by the more accurate micromechanical finite element model using the ABAQUS finite element package along with a user defined material subroutine (UMAT) for elastic-viscoplastic crystal plasticity theory [33].

Simulation of 0.2% plastic strain in plane strain compression was used in order to

check the Taylor factors of all orientations on $\phi_2 = 45^o$ section in Euler space [87]. A set of crystals ($0<\phi_1<90^o$, $0<\phi<90^o$, $\phi_2=45^o$) with 5^o increments was used as an initial set of orientations for the Taylor factor simulation by the Taylor model. For the micromechanical finite element simulation the same set of crystals as in Taylor model was randomly arranged in a mesh of cube shaped grains, (Figure 11a).

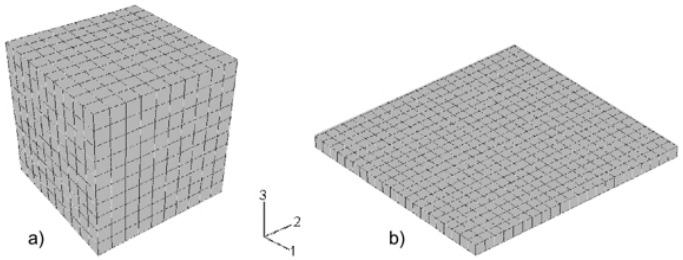

Figure 11: Finite element mesh with C3D8 elements used in: a) cubical mesh for Taylor factor calculations and light deformation simulations, b) single-layer mesh for heavy plane strain deformation simulation of columnar grained sample.

In addition, simulations also investigated a further important component of the proposed hypothesis. Since the lambda fiber is not a texture component that is stable in BCC metals under plane strain compression (or rolling), it was important to establish how quickly the lambda fiber grains rotate away towards the usual rolling texture components: the alpha and gamma fibers. Simulation of 10% plane strain deformation was performed in crystals that have orientations close to lambda fiber in order to compare their orientation stability, which was quantified here using the amount of lattice rotation produced by this strain. Orientation stability of lambda fiber was also compared with alpha fiber which is nearly stable during rolling deformation. Crystals orientations that lie 9^o and 18^o away from both the ideal lambda fiber ($0<\phi_1<90^o$, $\phi=0^o$) and the ideal alpha fiber ($\phi_1=0^o$, $0<\phi<90^o$) projected on the $\phi_2=45^o$ section were the focus of these studies.

These matched the experimentally observed deviations from the ideal lambda fiber in the samples. The micromechanical finite element simulation with the randomly assigned orientations of near lambda and alpha fibers in the mesh of cube shaped grains (Figure 11a) was used to supplement the Taylor model.

Furthermore, the change of texture for the initial heavy rolling reduction was also simulated by both models for a directionally solidified ingot of Fe-3%Si plane strain compressed 80%. The directionally solidified alloy had an even stronger initial lambda fiber texture than the continuously cast ingot. For simulation of the columnar structure, a single-layered mesh (Figure 11b) was used in the micromechanical finite element model.

In the Taylor factor maps (Figure 12) for the orientations in the ϕ_2=45^o section obtained by both Taylor and finite element modeling along the edge (ϕ=0^o) lies the lambda fiber (Figure 1b and Figure 4).

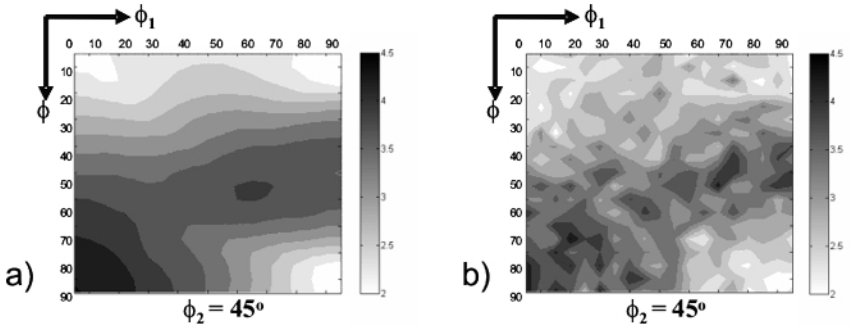

Figure 12: Taylor factor (M) maps for orientations on the ϕ_2 = 45^o section obtained by: a) Taylor model, b) Micromechanical finite element model.

The Taylor model (Figure 12a) shows orientations with <001> normal to the rolling plane do have low values of Taylor factor (M≈2), though with a somewhat higher value near cube, <001>{100}, at ϕ_1=45° (M≈2.5). The only other orientation with such a low value

of Taylor factor is the Goss orientation, {011}<100>, at $\phi=\phi_1=90°$. These results are also confirmed by the more physically valid micromechanical finite element model (Figure 12b). The results in Figure 12a are, as would be expected, similar to the results reported earlier for the variation of Taylor factor along the alpha fiber [18].

Both Taylor and micromechanical finite element models give similar results in predicting crystal rotations after 10% of plane strain deformation for a selected range of initial orientations, those 9° and 18° away from both the lambda and alpha fibers on the $\phi_2=45^o$ section (Figure 13).

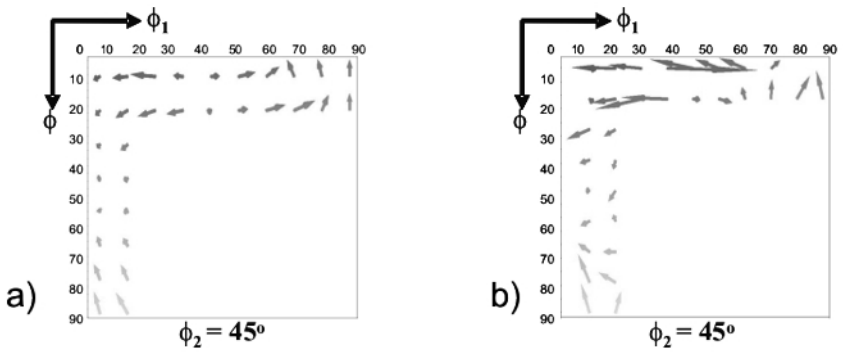

Figure 13: Modeled crystal rotations seen on the $\Phi_2 = 45^o$ section for 10% reduction by: a) Taylor model, b) Micromechanical finite element model.

Orientations close to cube component of the lambda fiber are unstable on rolling and tend to move towards rotated cube ($\phi_1=0°$ or $\phi_1=90°$) which is common for both lambda and alpha fibers. The near alpha orientations show small rotations, a not surprising result as this fiber is a known stable BCC rolling texture as it appears to be in both models.

Texture evolution in the directionally solidified sample with the strong lambda fiber, after plane strain compression, with the strain equivalent to that of heavy rolling reduction of continuously cast sample, was experimentally measured and compared with

predictions from both the Taylor and micromechanical finite element models (Figure 14). Simulation results were carried out for a directionally solidified ingot of Fe-3%Si that had an even stronger initial lambda fiber than that used in the present experiments. The actual measured columnar grain orientations were used in these simulations.

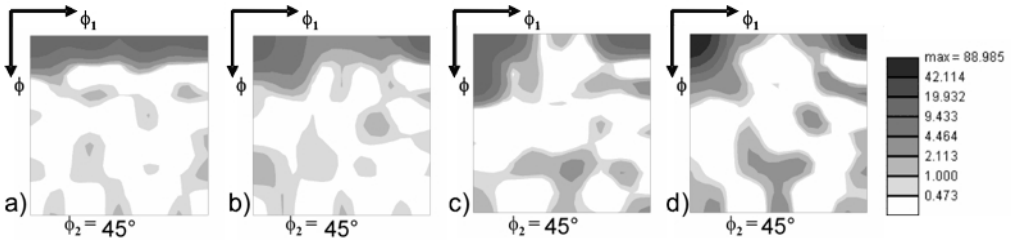

Figure 14: Textures of samples: a) as-cast, b) after plane strain compression experiment, c) predicted by Taylor model, d) predicted by finite element model after true strain of 1.6.

Both models show that orientations close to cube component of the lambda fiber are rotated towards rotated cube. In addition, while the Taylor model predicted the strengthening of the alpha fiber component near {112}<110>, the micromechanical finite element model predicted only the rotated cube component with high intensity. In comparison with the experimental measurements both models succeed rather well in predicting the development of the deformed texture. Despite the modeled instability of the lambda fiber much of it is retained even after heavy plane strain compression. Some of the lambda fiber grains must be retained after heavy rolling and then recrystallization for the texture to be recovered by the later light rolling and annealing steps.

5.3 Nanoindentation Experiment

For the proposed hypothesis that lambda grains have low Taylor factor associated with low stored energy and therefore recrystallize by strain induced boundary migration

mechanism after light deformation it is important to extract information about the orientation dependence of the stored energy in the deformed grains and verify hypothesis. To that end, a new approach has been developed in close collaboration with Kalidindi and Pathak [105] for converting the load-displacement data measured by nanoindentation into indentation stress-strain curves from which the stored energy can be extracted in the term of the yield strength. This new methodology outlined below involves a novel procedure for establishing the effective zero-load and zero-displacement point in the raw load-displacement dataset and the use of the continuous stiffness measurement (CSM) data.

5.3.1 Zero-Load and Zero-Displacement

Using the previously established definitions of the indentation stress (Eq. (3.15)) and indentation strain (Eq. (3.16)) the following step in the analysis of the raw data is an estimation of the point of initial contact (Effective zero point) in the load-displacement dataset. This includes identification of the point corresponding to zero-load and zero-displacement, which strongly affects the indentation stress and indentation strain, especially during the initial elastic loading. Problem of defining the point of initial contact has been discussed in the literature [106].

In this study, establishing of the zero-load and zero-displacement has been done through a regression analysis of the initial elastic loading segment in the measured load-displacement curve and subsequent fitting to the expected relationships obtained from Hertz's theory. Therefore, "effective" point of initial contact is identified rather than the "actual" point of initial contact, giving an advantage to eliminate surface conditions, such as surface roughness or the presence of an oxide layer.

During nanoindentation measurements the load signal P, displacement signal h, and the elastic stiffness signal S, can be recorded (S can be measured independently when the CSM option is used). Let P^* and h^* represent the values of the load and displacement signals at the actual point of initial contact (P^* and h^* are not necessarily zero after the MTS Testworks® software performs its default compliance and other corrections). According to the Hertz theory, in the elastic loading segment, the three signals measured in spherical indentation should be related as following:

$$S = \frac{3P}{2h_e} = \frac{3\left(P - P^*\right)}{2\left(h_e - h^*\right)}, \tag{5.1}$$

Eq. (5.1) can be rearranged as following:

$$P - \frac{2}{3}Sh = -\frac{2}{3}Sh^* + P^*. \tag{5.2}$$

The left-hand side of the Eq. (5.2), which contains experimentally measured values of P, S and h, can be plotted against S. By doing so, a linear relationship is obtained where slope is equal to -2/3h* and the intercept with the ordinates is equal to P* (Figure 15).

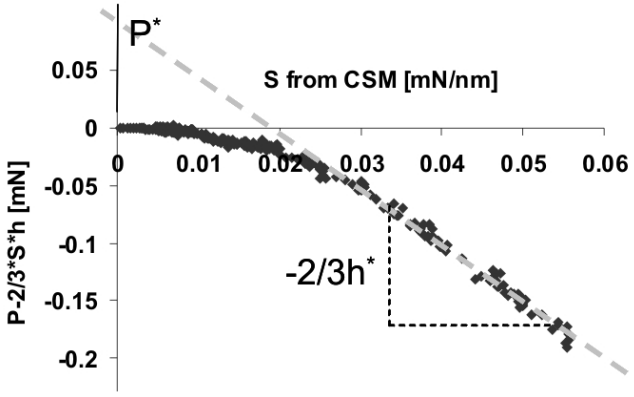

Figure 15: New method for identification of the effective zero-point based on the straight portion of the line, shown in the plot, used to estimate zero-load and zero-displacement.

A linear regression analysis can be used to accurately identify the point of the effective initial contact, while ensuring that the corrected data is consistent with the Hertz's theory. An advantage of the developed approach is that this method does not require any estimate of either R_{eff} or E_{eff}. An additional advantage of this new methodology for establishing the effective zero point is that very reasonably looking indentation stress-strain curves can be obtained when compared with the curves using the default zero point where unrealistic spikes usually occur in the initial loading and obscure yield point (Figure 16).

In this study, the procedures and concepts described above have been applied to experimental data obtained by using a MTS nanoindenter (XP system equipped with the CSM attachment) with a 13.5 micron radius spherical diamond tip.

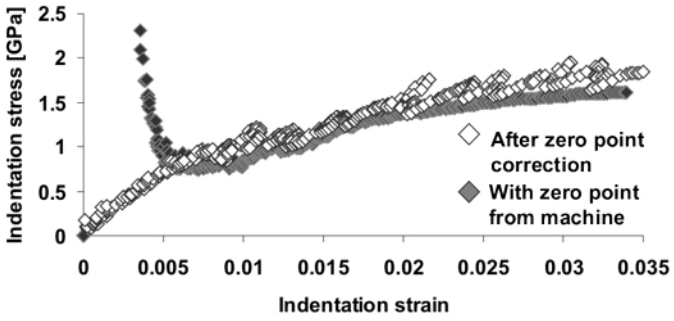

Figure 16: Example of indentation stress-strain curves with the developed zero point correction and default zero point from the machine.

5.3.2 Indentation Taylor-like Factor

Initially, a sample with the equiaxed and randomly oriented grain structure (obtained from the chill zone of directionally solidified electrical steel) was used to establish the intrinsic orientation dependence of indentation yield strength, that is, the indentation Taylor-like factor $\sigma_{ind}(g,0)$. In this notation, σ_{ind} represents the indentation

yield strength defined from the indentation stress-strain curve and g and 0 denote grain orientation and annealed state of the sample (zero cold work), respectively.

Eleven grains were identified in the sample (Figure 17a) and their orientations are shown in the standard stereographic triangle (Figure 17b) using the same colors.

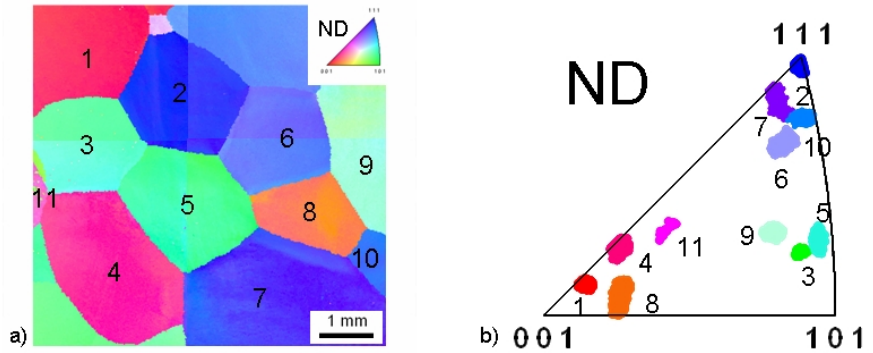

Figure 17: a) ND IPF map of the equiaxed grain structure in as-cast state, b) standard stereographic triangle showing orientation of the grains.

At least five nanoindentation measurements were carried in each grain and indentation stress-strain curves were extracted following the procedure described above (Figure 18). Some of the extracted indentation stress-strain curves (Figure 18b) had pop-ins (linear increase in indentation stress followed by both sudden drop in indentation stress and large increase in indentation strain). Back extrapolation was used to extract the indentation yield strength. It was observed that occurrence of pop-ins is stochastic which was also found in other BCC and FCC metals by Pathak (current research at Drexel). It is proposed that dislocation-free regions in the as-cast material were probed under the indenter and starvation of dislocation is believed to occur until the dislocations in the vicinity are induced to slip by increasing indentation stress.

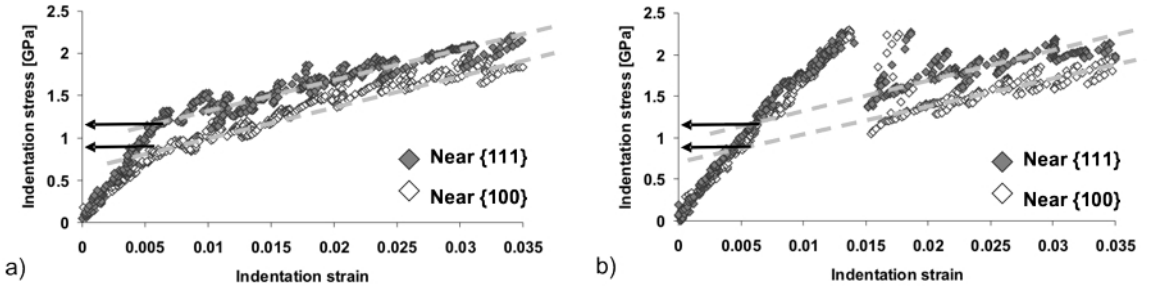

Figure 18: Example of indentation stress-strain curves a) without pop-ins, b) with pop-ins showing differences in indentation yield strength in the as-cast structure.

The extracted intrinsic orientation dependence of indentation yield strength (indentation Taylor-like factor) $\sigma_{ind}(g,0)$ and effective indentation modulus E_{eff} is shown in Table 3.

Table 3: Extracted average indentation yield strength and average effective indentation modulus from indentation stress-strain curves for as-cast equiaxed grains.

As-cast equiaxed grains							
G	ϕ_1, ϕ, ϕ_2	GOS	[001] from ND	[100] from RD	$\sigma_{ind}(g,0)$ [GPa]	E_{eff} [GPa]	E_{eff}/E_{av}
1	237, 9, 56	1.35	8.8	25.0	0.85 ±0.03 (0.02)	173.2 ±2.47 (1.10)	0.90
2	341, 54, 47	1.14	41.6	12.4	1.13 ±0.04 (0.02)	202.9 ±4.59 (2.05)	1.07
3	3, 41, 75	1.22	53.4	37.8	1.09 ±0.04 (0.02)	194.0 ±2.93 (1.31)	1.02
4	237, 16, 50	1.48	16.5	22.1	0.93 ±0.04 (0.02)	181.2 ±1.07 (0.53)	0.95
5	296, 44, 75	1.98	44.4	42.5	1.07 ±0.01 (0.01)	191.1 ±1.50 (0.86)	1.00
6	141, 45, 56	1.15	44.3	334.2	1.10 ±0.02 (0.01)	195.9 ±1.90 (1.34)	1.03
7	19, 49, 47	2.04	48.7	33.5	1.12 ±0.02 (0.01)	199.3 ±1.25 (0.51)	1.05
8	360, 14, 81	1.64	12.8	10.1	0.90 ±0.06 (0.03)	178.3 ±1.24 (0.61)	0.94
9	51, 39, 68	0.84	38.1	35.9	1.06 ±0.02 (0.01)	190.5 ±3.05 (2.15)	1.00
10	177, 49, 54	0.87	49.7	39.1	1.12 ±0.13 (0.06)	197.7 ±2.06 (1.03)	1.04
11	260, 24, 55	1.55	24.0	48.9	1.00 ±0.06 (0.03)	189.6 ±1.26 (0.89)	0.99

For each grain orientation is given in terms of the three Bunge-Euler angles, in-grain misorientation is calculated as the average misorientation between all data points in the grain (GOS). Misorientations of the grains from the sample reference frame (ND and RD) are calculated as well. Values in brackets, given in the table under the average indentation yield strength and average effective indentation modulus values represent the standard error of the mean. Standard error of the mean (SEM) is calculated with the standard deviation (SD) because SEM quantifies accuracy of the mean value while SD usually quantifies scatter between the measurements (it is expected that nanoindentation values vary between different locations). The two are related such that $SEM = SD/\sqrt{n}$ where n represents the number of measurements (n=5). The obtained range and values for effective indentation moduli is in remarkably good agreement with the data from Vlassak and Nix model [107] obtained from nanoindentation load-displacement data for three orientations {100}, {110} and {111} while accounting for elastic anisotropy (Figure 19).

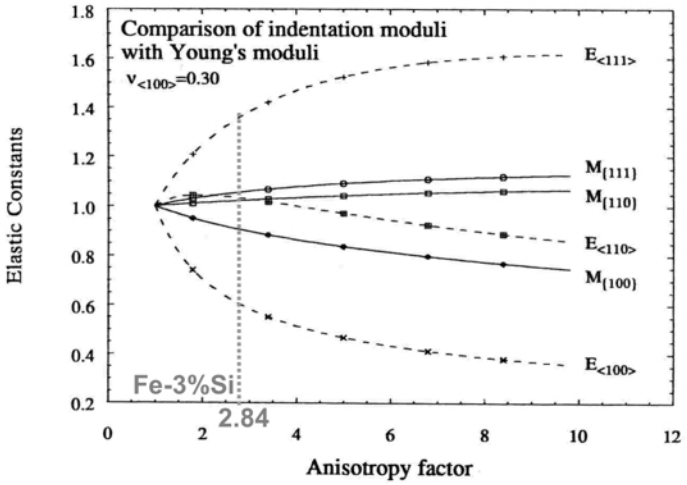

Figure 19: Comparison of indentation moduli M with the Young's moduli E for three different orientations as a function of elastic constants (Young's modulus and Poisson's ratio in the cube directions) and anisotropy factor [128]. Anisotropy factor for electrical steel is calculated and extracted range for indentation moduli is in very good agreement with the experimentally obtained values.

The obtained range of indentation moduli is 17% which is in very good agreement with 15% obtained by Vlassak and Nix (Figure 19). Also the average value of E_{eff}=190.34 [GPa] is close to that expected for non-textured Fe-3%Si steel [108].

Moreover, the experimentally obtained indentation yield strength values from as-cast sample were used to interpolate the indentation yield strength surface as a function of orientation expressed in terms of two Bunge-Euler angles ϕ and ϕ_2 (Figure 20).

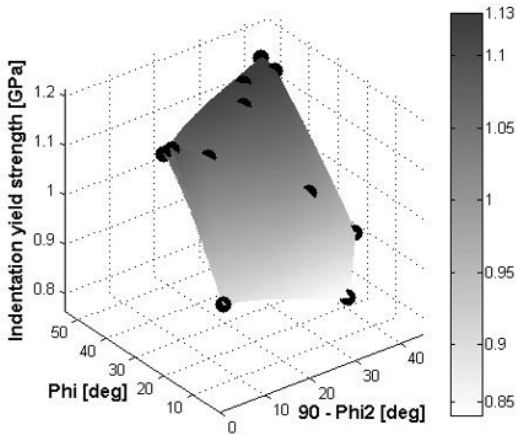

Figure 20: Interpolated indentation yield strength surface as a function of two Bunge-Euler angles from experimental measurements shown as the dark spheres.

With the generated indentation yield strength surface, it would be possible to extract the indentation yield strength values for other orientations that did not exist in the initial as-cast structure, but were developed later during deformation. This would allow considering an increase in indentation yield strength of deformed material due to an intrinsic increase in dislocation density (stored energy) alone, separating out the contribution from the intrinsic orientation dependence.

In order to characterize the evolution of deformed microstructure at the grain-scale level (in terms of local orientations and stored energies) plane strain deformation

was done in several stages and the microstructure was characterized after each deformation stage by combining OIM and nanoindentation techniques.

5.4 Plane Strain Compression Experiment

After establishing intrinsic orientation dependence of indentation yield strength in the as-cast structure (indentation Taylor-like factor) the next logical step was to verify that developed nanoindentation methodology can be also successfully used for characterization of stored energy variation with orientation during deformation. A quick plane strain compression experiment was done in order to test the developed nanoindentation methodology for extracting the values of stored energy through the increase in indentation yield strength.

A sample of the directionally solidified electrical steel was compressed along the columnar growth of lambda grains in a channel die at room temperature using an Instron screw driven testing machine in three steps to height reductions of 60, 70 and 80% that correspond to true strains of 0.9, 1.2 and 1.6, respectively. Initially, bottom plate, side plates and plunger were lubricated with the graphite based grease upon which the fixture was assembled in the steel jacket. The compression and the constrained surfaces (surfaces perpendicular to ND and TD) of the sample where also lubricated with the graphite based grease and then covered by a layer of Teflon (0.1 mm thick) to minimize friction. After that, sample was placed in the fixture such that the direction of columnar grains is parallel with the compression axis. The same was repeated for the other deformation steps. After the final deformation step one grain was carefully characterized by OIM. The selected grain (Figure 21) had developed several orientation fields that were used for nanoindentation measurements.

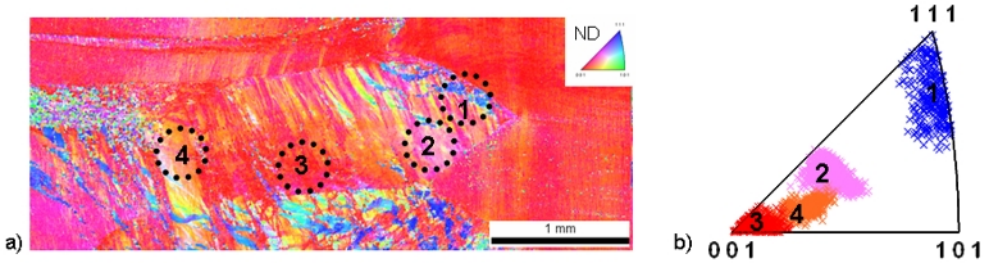

Figure 21: a) ND IPF map of the columnar grain sample after plane strain compression to true strain of 1.6, b) standard stereographic triangle showing developed orientations within the grain used for nanoindentation measurements (circled regions in the IPF map).

From the nanoindentation measurements the indentation yield strength $\sigma_{ind}(g_f,\varepsilon_{cw})$ is extracted in the selected regions of deformed grain. In this notation g_f denotes the final grain orientation developed during plane strain compression and ε_{cw} denotes cold work state. The extracted values are shown in Table 4. In addition, developed new orientations within the grain (from initial lambda grain) were considered and the indentation Taylor-like factors for new orientations $\sigma_{ind}(g_f,0)$ were extracted from the indentation yield strength surface and given in Table 4. In this notation, g_f and 0 denote the final grain orientation developed during plane strain compression and assuming the presence of that orientation in an annealed state (before the previous cold work), respectively. Therefore, the increase in the indentation yield strength after cold work is given as following:

$$\Delta\sigma_{ind} = \left[\sigma_{ind}(g_f,\varepsilon_{cw}) - \sigma_{ind}(g_f,0)\right], \qquad (5.3)$$

In a single phase high solute Fe-Si alloys a total resistance to the plastic flow (τ) is due to solute resistance (τ_{ss}) and dislocation resistance (τ_ρ), i.e. $\tau = \tau_{ss} + \tau_\rho$. The increase in plastic flow during deformation is, can be assumed, mostly due to decrease of the free slip length caused by the increase in dislocation density and the increase in indentation yield strength can be related to the change in critical resolved shear stress ($\Delta\tau_{CRSS}$) as:

$$\frac{\Delta\sigma_{ind}}{\sigma_{ind}(0)} = \frac{\Delta\tau_{CRSS}}{\tau_{CRSS}(0)}, \tag{5.4}$$

where $\sigma_{ind}(0) = \sigma_{ind}(g_f,0)$ and $\tau_{CRSS}(0)$ is the critical resolved shear stress for initial as-cast structure and it can be calculated from the initial yielding during plane strain compression and initial Taylor factor, i.e. $\tau_{CRSS}(0) = \sigma_y/M$. The initial yielding σ_y=460 [MPa] is determined from the plane strain compression true stress-strain curve (Figure 23a) and Taylor factor M=2.3 is calculated for the initial as-cast structure. The change in the critical resolved shear stress ($\Delta\tau_{CRSS}$) due to increase in indentation yield strength can be calculated from Eq. (5.4) and a measure of stored energy due to an intrinsic increase in dislocation density, can be expressed as following:

$$\rho_{ind} \approx \left[\frac{\Delta\tau_{CRSS}}{Gb}\right]^2. \tag{5.5}$$

where for steel shear modulus G=80 [GPa] and Burgers vector b=0.3x10^{-9} [m]. Estimated values of stored energy (Eq. (3.2)) from ρ_{ind} using Eq. (5.5) are given in Table 4. It can be noticed that new orientations (further away from lambda fiber) have higher indentation yield strength.

Table 4: Extracted values of indentation yield strength, change in critical resolved shear stress and dislocation density after plane strain compression to true strain of 1.6.

Locations in columnar grain deformed by plane strain compression (ε = 1.6)								
L	ϕ_1, ϕ, ϕ_2	GOS	[001] from ND	[100] from RD	$\sigma_{ind}(g_f,\varepsilon_{cw})$ [GPa]	$\sigma_{ind}(g_f,0)$ [GPa]	$\Delta\tau_{CRSS}$ [MPa]	ρ_{ind} x10^{12} [m^{-2}]
1	112, 49, 54	6.51	47.7	42.3	1.69 ±0.06 (0.03)	1.12	102	18
2	326, 23, 58	4.35	23.9	30.5	1.46 ±0.07 (0.04)	0.99	95	16
3	259, 4, 84	3.70	5.9	21.2	1.27 ±0.04 (0.02)	0.85	99	17
4	263, 16, 74	4.04	16.2	28.4	1.37±0.06 (0.03)	0.92	98	17

Indentation stress-strain curves for selected orientations in the deformed lambda grain clearly show the increase in the indentation yield strength when compared with the indentation stress-strain curve from as-cast orientation (Figure 22). Therefore, the observed difference in yield strength between different orientations developed during deformation has confirmed the capability of developed methodology for characterization of stored energy as a function of orientation during deformation.

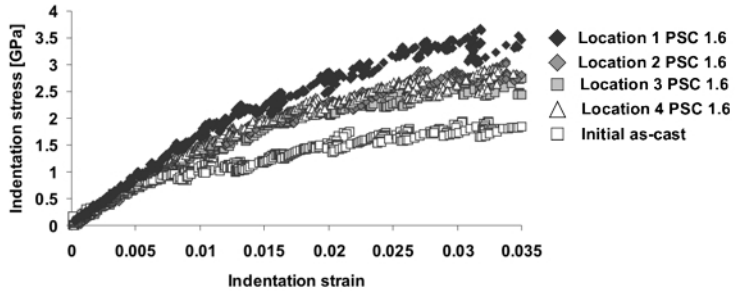

Figure 22: Extracted indentation stress-strain curves from differently oriented regions within the lambda grain deformed to true strain of 1.6 and from the initial as-cast state.

Furthermore, it can be also observed that strain hardening in the indentation stress-strain curves (Figure 22) is much higher when compared with the true stress-strain curves from plane strain compression experiments (Figure 23a) where in the first deformation stage the strain hardening is high while in the second and the third deformation stage the strain hardening is very small. The drop in the flow stress between the deformation stages is due to the applied lubrication at the beginning of each deformation step. Extracted values of yield strength and strain hardening from indentation stress-strain curves and plane strain compression true stress-strain curves are given in Table 5.

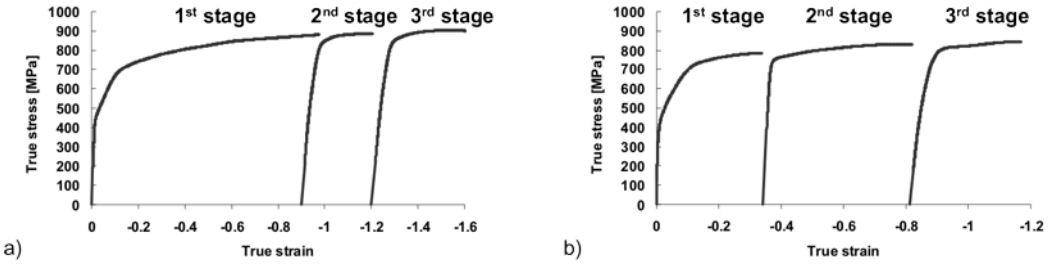

Figure 23: True stress-strain curves for the three stages of the plane strain compression experiments to: a) true strain of 1.6, b) true strain of 1.21.

Table 5: Extracted: 5a) yield strength and 5b) strain hardening from nanoindentation (NI) stress-strain curves and plane strain compression (PSC) true stress-strain curves.

	Yield strength [MPa]	
PSC	As-cast (AC)	450
	3rd def. stage	850
NI	As-cast (AC)	850
	After ε_{psc}=1.6	1270

	Strain hardening dσ/dε [MPa]			
PSC	$\varepsilon_{psc\ (I)}$ 0.02-0.035	$\varepsilon_{psc\ (I)}$ 0.8-0.9	$\varepsilon_{psc\ (II)}$ 1.1-1.2	$\varepsilon_{psc\ (III)}$ 1.4-1.6
	3333	100	50	35
NI	As-cast		After ε_{psc}=1.6	
	$\varepsilon_{ind\ (AC)}$ 0.01-0.02	$\varepsilon_{ind\ (AC)}$ 0.02-0.035	$\varepsilon_{ind\ (PSC)}$ 0.01-0.02	$\varepsilon_{ind\ (PSC)}$ 0.02-0.035
	50000	22600	75000	33300

In this quick experiment it was not known when the orientation fields have been developed during deformation. In order to document the microstructure evolution during deformation another sample of directionally solidified steel was deformed in three stages to height reductions of 30, 55 and 70% that correspond to true strains of 0.34, 0.81 and 1.21, respectively (Figure 23b). The results after each deformation step are shown below.

5.4.1 First Deformation Stage

Initial OIM scans were obtained from multiple scans taken and placed next to each other. It was found that the top side of the sample (side that was further away from a

chill zone during casting) contained more of the grains that matched with the grains on the other (bottom) side. Therefore, after each deformation step OIM map of the entire top surface was generated with the focus on the grains labelled 1 through 8 which were entirely surrounded by grains that were in contact with a channel die (Figure 24).

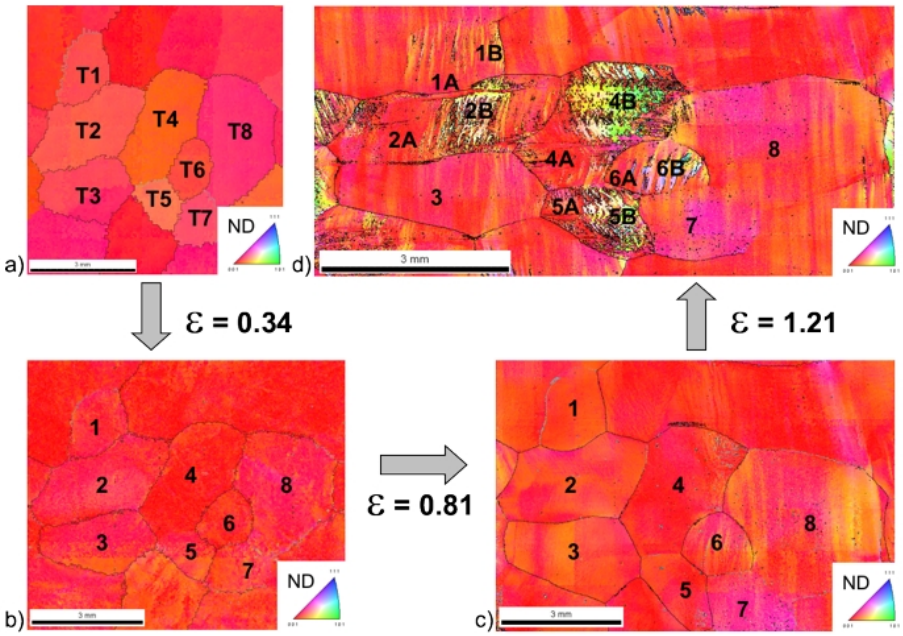

Figure 24: ND IPF maps of the top surface showing a) as-cast microstructure, and microstructure after plane strain compression to true strain of b) 0.34, c) 0.81 and d) 1.21.

After the first deformation step the microstructure did not change significantly (Figure 24b). Slight variations in colors within the grains indicated small in-grain misorientation developed in this deformation stage.

Texture evolution during deformation was compared with a finite element model (Figure 25). Initial texture was strengthened and the misorientation from the ideal lambda fiber has decreased from 11^{o} to 6^{o}. The model predicted larger rotations and weakening of the cube orientation (Figure 25-IIb).

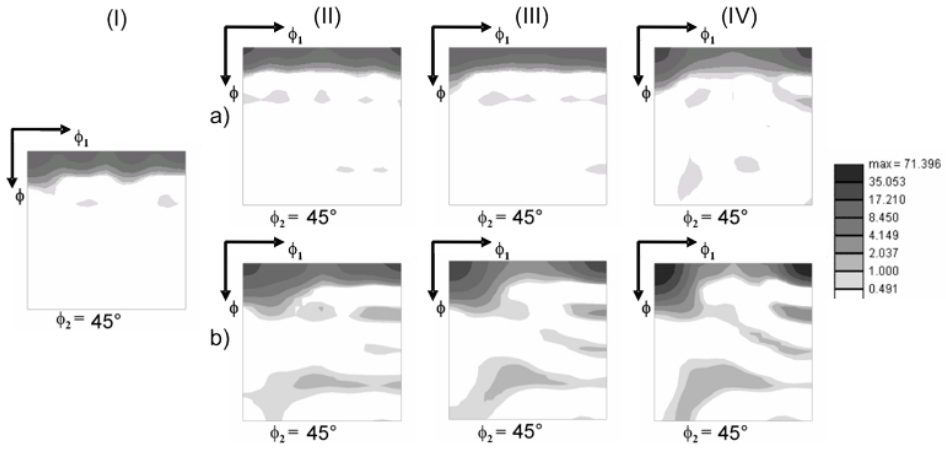

Figure 25: ODF plots of (I) initial texture and after plane strain compression a) experiment, b) simulation to true strain of (II) 0.34, (III) 0.81 and (IV) 1.21.

From indentation yield strength surface the indentation Taylor-like factors were extracted for columnar grains and given in Table 6. After the first deformation step nanoindentation was carried in each grain and the indentation yield strength $\sigma_{ind}(g_f,\varepsilon_{cw})$ values were extracted from the indentation stress-strain curves. Using the Eq. (5.5) the increase in stored energy is calculated and the obtained values are shown in Table 7.

Table 6: Extracted indentation yield strength for as-cast columnar grains.

As-cast columnar grains					
Grain	ϕ_1, ϕ, ϕ_2	GOS	[001] from ND	[100] from RD	$\sigma_{ind}(g,0)$ [GPa]
1	151, 7, 72	0.65	7.3	40.6	0.85
2	10, 9, 59	0.62	8.5	20.8	0.86
3	166, 9, 56	0.96	8.0	43.4	0.85
4	280, 6, 85	0.79	6.1	8.1	0.85
5	189, 13, 79	0.61	11.2	3.1	0.89
6	221, 7, 76	0.70	6.0	27.4	0.85
7	343, 10, 63	0.63	10.2	43.5	0.87
8	343, 11, 53	0.64	9.5	34.9	0.87

Table 7: Extracted values of indentation yield strength, change in critical resolved shear stress, dislocation density and calculated strain path average Taylor factors (M_{spa}) after the first deformation stage.

Deformed columnar grains by plane strain compression ($\varepsilon = 0.34$)									
G	ϕ_1, ϕ, ϕ_2	GOS	[001] from ND	[100] from RD	$\sigma_{ind}(g_f,\varepsilon_{cw})$ [GPa]	$\sigma_{ind}(g_f,0)$ [GPa]	$\Delta\tau_{CRSS}$ [MPa]	ρ_{ind} x10^{12} [m^{-2}]	M_{spa}
1	333, 5, 61	1.87	4.7	34.0	1.29 ±0.05 (0.02)	0.85	107	20	2.1
2	324, 5, 50	3.18	5.8	15.4	1.24 ±0.11 (0.05)	0.85	95	16	2.3
3	339, 5, 61	2.74	5.5	39.7	1.23 ±0.07 (0.03)	0.85	93	15	2.2
4	267, 1, 93	3.12	2.2	3.0	1.28 ±0.05 (0.02)	0.85	105	19	2.5
5	294, 6, 64	2.75	6.0	5.7	1.24 ±0.04 (0.02)	0.86	91	15	2.5
6	308, 3, 76	2.26	3.5	23.8	1.22 ±0.10 (0.04)	0.85	90	14	2.2
7	335, 6, 68	2.80	6.2	42.8	1.23 ±0.11 (0.05)	0.86	90	14	2.3
8	333, 5, 61	2.63	5.7	40.3	1.29 ±0.14 (0.06)	0.85	107	20	2.2

5.4.2 Second Deformation Stage

Following the second deformation step the orientation fields (running parallel to TD) were developed in grains no.6 and no. 8, while other grains retained homogeneous orientations (Figure 24c). The experimentally observed texture remained stable even after the increased deformation during the second deformation stage, while the finite element model predicted further rotations towards the more stable rotated cube orientation (Figure 25-III). Again, the developed changes in orientation were considered and the indentation Taylor-like factors $\sigma_{ind}(g_f,0)$ for new orientations were extracted from the indentation yield strength surface plot. Indentation measurements were repeated in each grain and the indentation yield strength $\sigma_{ind}(g_f,\varepsilon_{cw})$ values were obtained from the indentation stress-strain curves. The increase in stored energy is calculated and values are shown in Table 8.

Table 8: Extracted values of indentation yield strength, change in critical resolved shear stress, dislocation density and calculated strain path average Taylor factors (M_{spa}) after the second deformation stage.

Deformed columnar grains by plane strain compression ($\varepsilon = 0.81$)									
G	ϕ_1, ϕ, ϕ_2	GOS	[001] from ND	[100] from RD	$\sigma_{ind}(g_f,\varepsilon_{cw})$ [GPa]	$\sigma_{ind}(g_f,0)$ [GPa]	$\Delta\tau_{CRSS}$ [MPa]	ρ_{ind} x10^{12} [m^{-2}]	M_{spa}
1	148, 5, 90	1.93	4.6	33.7	1.32 ±0.03 (0.01)	0.85	114	23	2.1
2	36, 5, 72	4.11	5.9	16.6	1.33 ±0.08 (0.03)	0.85	117	24	2.3
3	155, 5, 76	3.27	6.2	40.1	1.34 ±0.08 (0.03)	0.85	119	25	2.2
4	311, 3, 50	4.80	3.9	5.3	1.37 ±0.11 (0.02)	0.85	127	29	2.5
5	324, 4, 46	3.31	4.8	3.3	1.37 ±0.05 (0.02)	0.85	127	29	2.5
6	325, 7, 65	4.31	7.5	30.0	1.42 ±0.07 (0.03)	0.86	135	35	2.2
7	357, 12, 46	3.97	12.6	43.2	1.40 ±0.04 (0.02)	0.88	122	26	2.3
8	147, 8, 72	5.06	8.5	39.6	1.37 ±0.10 (0.04)	0.87	119	25	2.2

5.4.3 Third Deformation Stage

After the final deformation step large misorientations were developed within the grains and most of them (except grains no. 3, 7 and 8) split in several deformation bands with the repeating orientation fields (Figures 24d and 26). Grain no.1 split in two bands, 1A and 1B with about 6^o and 14^o away from the lambda fiber, respectively. The left part of the grain no. 2 has deformed uniformly (2A), while in the right part of the grain deformation bands with the repeating orientation fields have developed (2B). The uniformly deformed region (2A) stayed close to the lambda fiber while the developed bands (2B) were about 27^o away. Grain no.3 has deformed uniformly with the orientation close to the rotated cube.

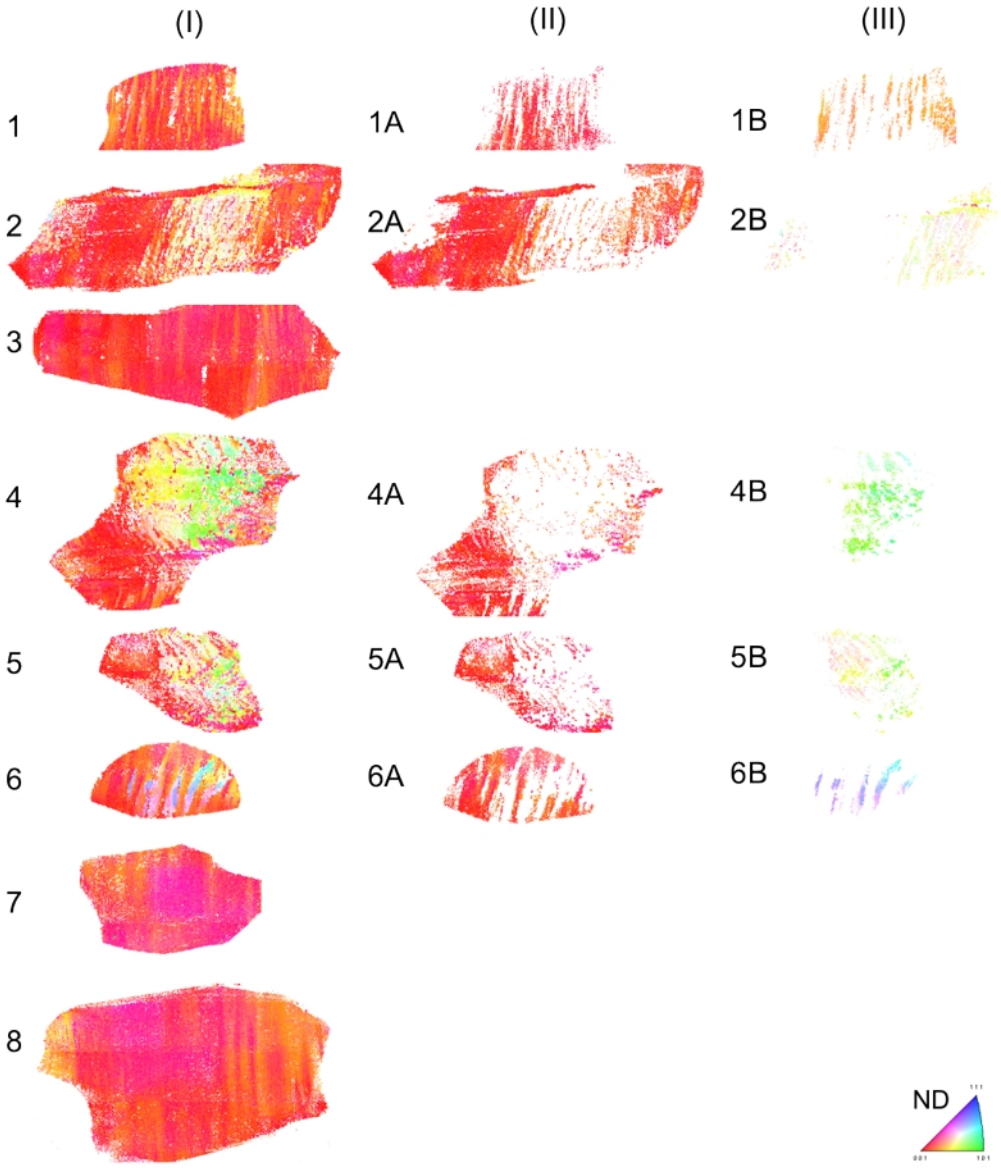

Figure 26: ND IPF maps of (I) individual grains after the third deformation step showing fragmentation of the grains with repeating orientation fields (II) close to the lambda fiber, (III) distant from the lambda fiber.

The bottom part of grain no. 4 has deformed uniformly (4A), while in the top part of the grain deformation bands with the repeating orientation fields have developed (4B) that were about 7^{o} and 35^{o} away from the lambda fiber, respectively. Grain no.5 also had homogeneously deformed left part (5A) and regions with the deformation bands with the repeating orientation fields (5B) in the right part of the grain. The homogeneously

deformed part of the grain was about 8^{o} away from the cube component and the part of the grain with bands with the repeating orientation fields was about 36^{o} away from lambda fiber. Most of the grain no. 6 was uniformly deformed (6A) and just a several bands with the repeating orientation fields (6B) have spanned the grain. Uniformly deformed region was about 9^{o} away from the rotated cube, while the developed bands were about 36^{o} away from the lambda fiber. Grains no. 7 and 8 deformed uniformly and they have their orientations close to the rotated cube.

The texture developed after the last deformation step contained strengthened rotated cube and weakened cube orientation. The micromechanical finite element model predicted stronger rotated cube and weaker cube orientation (Figure 25-IV).

In the last stage of deformation, the developed changes in orientation in the split grains were considered for dominant orientation fields. Following the same procedure as previously described for preceding deformation steps the indentation Taylor-like factors for new orientations were extracted from the indentation yield strength surface and nanoindentation measurements were done in the developed orientation fields (Figure 26). The increase in indentation yield strength has increased further, but less so for orientation fields close to the lambda fiber and more so for orientation fields further away from the lambda fiber, particularly in grain no.6. The obtained values are shown in Table 9.

Extracted indentation stress-strain curves for the three deformation stages show increase in the indentation yield strength between the plane strain compression steps, however, the increase in the indentation yield strength is substantially larger in the new deformation bands developed during the third deformation stage (Figure 27).

Table 9: Extracted values of indentation yield strength, change in critical resolved shear stress, dislocation density and calculated strain path average Taylor factors (M_{spa}) after the third deformation stage.

Deformed columnar grains by plane strain compression ($\varepsilon = 1.21$)									
G	ϕ_1, ϕ, ϕ_2	GOS	[001] from ND	[100] from RD	$\sigma_{ind}(g_f,\varepsilon_{cw})$ [GPa]	$\sigma_{ind}(g_f,0)$ [GPa]	$\Delta\tau_{CRSS}$ [MPa]	ρ_{ind} x10^{12} [m^{-2}]	M_{spa}
1A	339,6,56	2.91	6.2	35.0	1.38 ±0.06 (0.03)	0.85	129	29	2.2
1B	246,15,82	2.85	14.5	343.3	1.47 ±0.09 (0.04)	0.91	127	28	2.2
2A	339,2,39	9.75	6.6	21.7	1.41 ±0.08 (0.03)	0.85	136	32	2.4
2B	266,26,81	4.34	27.1	30.0	1.53 ±0.05 (0.02)	0.99	113	22	2.6
3	342,6,57	5.01	7.3	38.9	1.37 ±0.11 (0.04)	0.86	123	26	2.2
4A	324,2,30	6.72	7.0	12.4	1.44 ±0.03 (0.01)	0.85	104	19	2.5
4B	272,37,84	5.11	35.2	35.5	1.59 ±0.13 (0.06)	1.06	104	19	2.7
5A	99,6,90	5.36	7.6	11.6	1.45 ±0.06 (0.03)	0.86	142	35	2.6
5B	288,27,70	4.98	28.3	27.6	1.55 ±0.09 (0.04)	1.00	114	23	2.7
6A	331,7,67	4.67	9.1	35.9	1.47 ±0.11 (0.05)	0.87	167	48	2.3
6B	122,58,72	3.86	36.0	44.3	1.78 ±0.13 (0.06)	1.08	134	31	2.5
7	346,12,57	4.41	12.6	43.0	1.41 ±0.08 (0.04)	0.89	121	25	2.3
8	167,10,53	5.42	9.3	40.9	1.42 ±0.09 (0.04)	0.87	124	27	2.2

Again, the strain hardening in the indentation stress-strain curves appeared to be high after each plane strain compression step, particularly in the deformation bands developed during the third stage of deformation. This becomes clearly apparent when compared with the plane strain compression true stress-strain curves (Figure 23b).

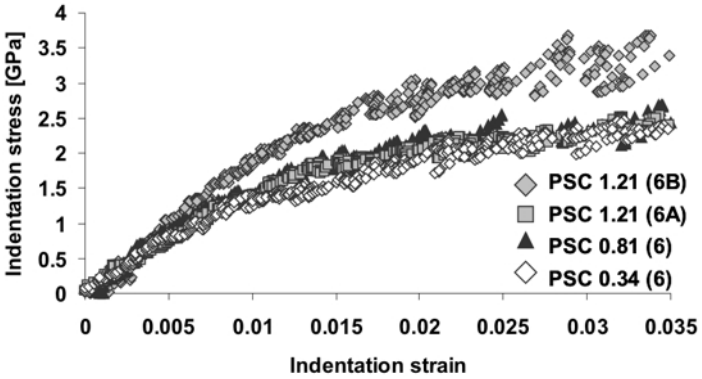

Figure 27: Examples of the extracted indentation stress-strain curves from grain no.6 for the three deformation steps including two different deformation bands developed during the third stage (6A and 6B).

The initial lambda fiber columnar grains remained partially stable during the three stage plane strain compression and the strain path average Taylor factor values did not change much during monotonic plane strain compression. Therefore, it was not possible to extract a clear relationship between the dislocation density and strain path average Taylor factor (Figure 28).

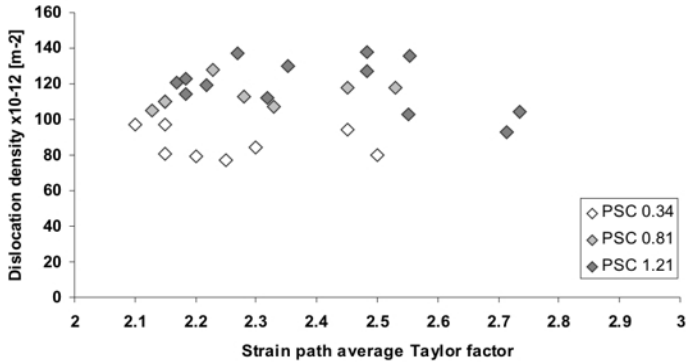

Figure 28: Plot of extracted dislocation density and strain path average Taylor factor.

5.5 Annealing Experiment

The sample that was initially used in plane strain compression to true strain of 1.6 was also used for annealing experiment. Sample was used for studying the formation of

recrystallized grains in the deformed structure during subsequent annealing and verifying experimental capability of extracting stored energy difference in partially annealed structure which plays an important role in development of the final microstructure.

Initially, one half of the deformed sample was used for establishing the annealing behaviour in terms of variation of the Vickers micro-hardness with the annealing time for a given temperature in a salt bath (Figure 29). The Vickers hardness values were obtained from multiple indentation sites in different grains using the load of 25 grams and indentation time of 15 seconds on Leco micro-hardness tester. From the established annealing curve in a salt bath, a time of 30 minutes was selected for partial annealing of the other half of the deformed sample (to obtain about 10% recrystallized structure).

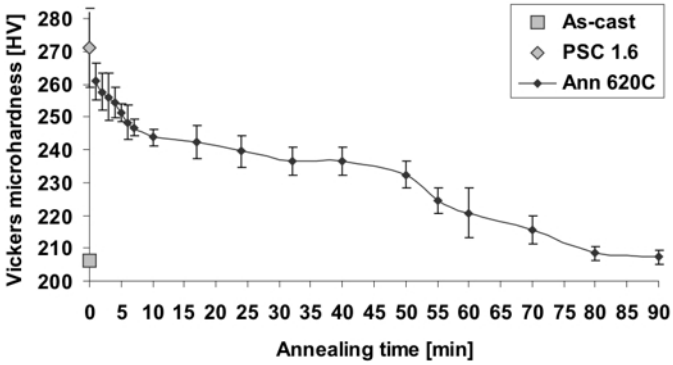

Figure 29: Variation of the Vickers micro-hardness in iron-silicon electrical steel, deformed in plane strain compression to true strain of 1.6, with time at 620^{o}C in salt bath.

Prior to the partial annealing, a high resolution OIM map (Figure 30a) was obtained from selected area comprised of both primary grain boundaries and transition bands developed during deformation (Figure 30c). The selected boundaries are high angle boundaries and possess high mobility and therefore new recrystallized grains should

preferentially form at those locations.

After annealing at 620°C for 30 minutes in salt bath the sample was polished and new high resolution OIM map (Figure 30b) was obtained from the same location. Two different regions in partially annealed microstructure were selected for nanoindentation measurements: (i) regions of individual recrystallized grains and (ii) well recovered but not recrystallized regions (Figures 30b and 30d).

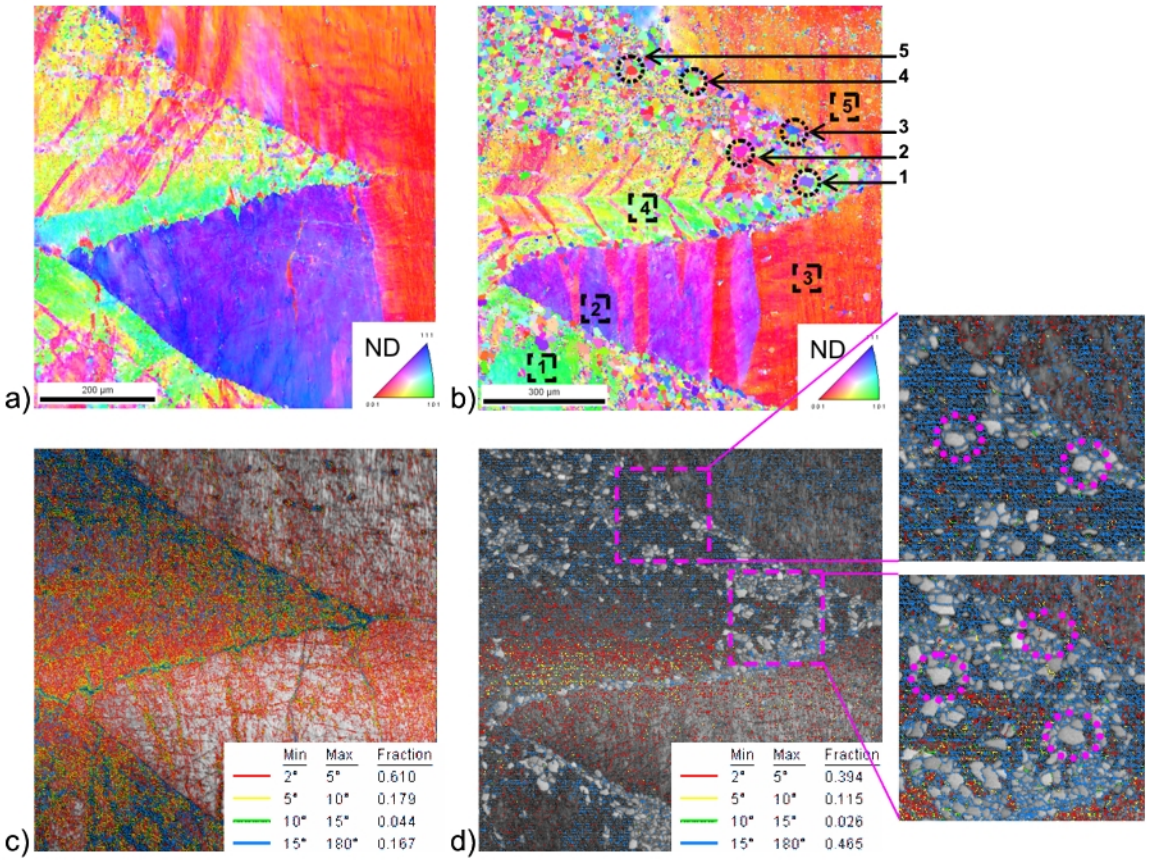

Figure 30: ND IPF maps of a) deformed sample, b) partially annealed sample (showing the selected recrystallized grains (circles) and well recovered regions (squares) for nanoindentation measurements) and grain boundary color maps for c) deformed sample, d) partially annealed sample with the insets showing high angle boundaries (more than 15° are colored blue) surrounding selected recrystallized for nanoindentation study.

Following the same nanoindentation methodology the indentation yield strengths were obtained for selected regions. The misorientations of selected grains no. 1, 2, 3, 4, and 5 (circled grains in Figure 30b) from adjacent regions were in the range of 25-61^{o}, 33-50^{o}, 42-58^{o}, 24-53^{o} and 21-57^{o}, respectively (magnified regions in Figure 30d).

The extracted values for the indentation yield strength of the recrystallized grains were very close to the values established for the as-cast equiaxed grain structure and are shown in Table 10.

Table 10: Extracted values of indentation yield strength, change in critical resolved shear stress, decrease in dislocation density and Taylor factor (M) after deformation followed by partial annealing in recrystallized grains.

Recrystallized grains in partially annealed structure									
G	ϕ_1, ϕ, ϕ_2	GOS	[001] from ND	[100] from RD	$\sigma_{ind}(g_f,\varepsilon_{cw})$ [GPa]	$\sigma_{ind}(g_f,0)$ [GPa]	$\Delta\tau_{CRSS}$ [MPa]	ρ_{ind} x10^{12} [m^{-2}]	M
R1	325,41,55	0.39	41.1	32.7	1.10	1.08	4	0.02	3.5
R2	216,22,51	0.39	22.3	15.2	1.03	0.98	10	0.2	2.9
R3	216,49,54	0.37	49.6	29.1	1.16	1.12	7	0.08	3.4
R4	288,38,82	0.33	37.7	37.9	1.08	1.05	6	0.06	4.1
R5	306,6,63	0.37	5.4	10.0	0.88	0.85	7	0.09	2.5

Extracted values of indentation yield strength from indentation stress-strain curves for recrystallized grains were comparable with the values obtained from as-cast structure. Therefore, values from recrystallized grains were included in the surface plot of indentation yield strength and new plot was generated (Figure 31). The new plot looks similar to original (Figure 20) but slightly shallow.

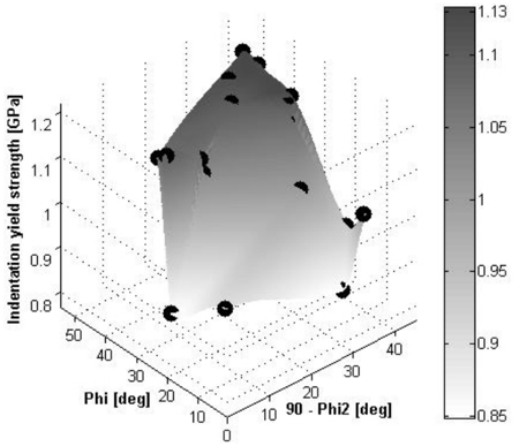

Figure 31: Interpolated indentation yield strength surface as a function of two Bunge-Euler angles from experimental measurements (original data from as-cast structure plus data from recrystallized grains) shown as the dark spheres.

The extracted values for the indentation yield strength of the selected well recovered regions (squared regions in Figure 30b) had somewhat larger values when compared with the values established for the as-cast structure and are shown in Table 11. Variation in stored energy between recovered regions is small to be compared with Taylor factors.

Table 11: Extracted values of indentation yield strength, change in critical resolved shear stress, decrease in dislocation density and Taylor factor (M) after deformation followed by partial annealing in recovered regions.

Well recovered regions in partially annealed structure									
L	ϕ_1, ϕ, ϕ_2	GOS	[001] from ND	[100] from RD	$\sigma_{ind}(g_f,\varepsilon_{cw})$ [GPa]	$\sigma_{ind}(g_f,0)$ [GPa]	$\Delta\tau_{CRSS}$ [MPa]	ρ_{ind} x10^{12} [m^{-2}]	M
r1	252,45,83	0.94	43.3	47.1	1.44 ±0.09 (0.04)	1.06	72	9	3.9
r2	281,35,45	2.42	36.1	46.2	1.40 ±0.12 (0.05)	1.03	72	9	3.8
r3	225,6,90	1.64	6.4	44.0	1.18 ±0.01 (0.02)	0.85	78	11	2.2
r4	262,34,79	1.95	34.5	39.3	1.38 ±0.12 (0.05)	1.02	71	9	3.7
r5	313,14,90	1.79	15.7	43.0	1.24 ±0.04 (0.02)	0.9	76	11	2.5

The extracted indentation stress-strain curves from selected recrystallized grains had large pop-ins (Figure 32). Back extrapolation was used to extract the indentation yield strength. In addition, well recovered locations 3 and 5 have also contained pop-ins in the indentation stress-strain curves and somewhat higher flow stresses (Figure 32). Indentation stress-strain curves from the other three well recovered locations 1, 2 and 4 did not exhibit pop-ins (Figure 33). Well recovered regions that exhibited pop-ins had smaller indentation yield strength values than regions that did not exhibit pop-ins.

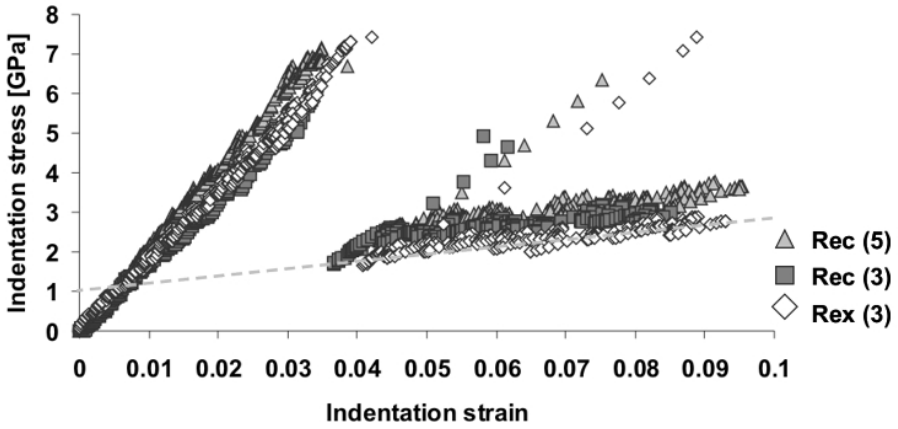

Figure 32: Examples of the extracted indentation stress-strain curves containing pop-ins in recrystallized grain no. 3 and well recovered regions no. 3 and 5.

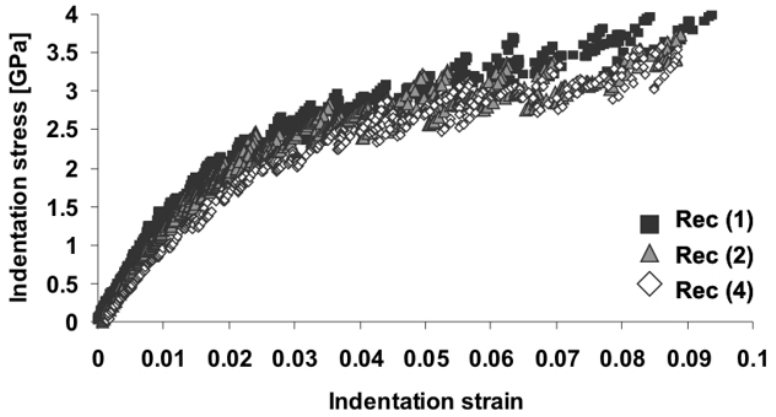

Figure 33: Examples of the extracted indentation stress-strain curves without pop-ins in well recovered regions no. 1, 2 and 4.

As mentioned earlier, the effect of pop-ins in the indentation stress-strain curves is believed to occur due to low dislocation density in the material. Therefore, during nanoindentation probing a dislocation-free region is probably probed under the indenter tip. The rise in indentation stress is expected to occur when the dislocation free region ("perfect" part of the crystal) is probed. Furthermore, once the dislocations present in the surrounding region start to sense the stress imposed by an indenter, it is believed that new dislocations are instantly generated once the indentation stress reaches critical value. This sudden burst of dislocations, it is believed, leads to observed substantially large increment in indentation strain. It also believed that an outburst of dislocations leads to a significant downward displacement of the surface under the indenter tip which leads to an elastic unloading. Although the tip is moving downward as well, the decrease in indentation load is larger than the decrease in contact due to elastic displacement of the surface upward. Elastic unloading is manifested with the drop in indentation strain observed in indentation stress-strain curve. The support to proposed idea is that the unloading slope (after the burst of dislocations) is very similar to the initial loading slope (before the burst of dislocations).

Nanoindentation technique was also used for grain boundary characterization of the as-cast grains (Figure 17). However, methodology for finding the effective zero-load and zero displacement point in the raw load-displacement data with the use of CSM data was not developed at the time of experiments. The results have to be verified with the now available better indentation technique. Nevertheless, according to the author preliminary results are very interesting and are outline in the appendix.

CHAPTER 6: DISCUSSION

Heavy deformation by rolling of continuously cast material with coarse columnar lambda fiber grain structure produced additional rotations of the crystals near the surface due, it can be assumed, to additional shear caused by friction between the sample and rolls (Figure 10-Ia). In the midplane section, where the plane strain condition is expected to be satisfied, the crystals stayed closer to the lambda fiber (Figure 10-Ib).

In addition, the individual large grains were more prone to break up during heavy deformation as indicated by the very heavy in-grain nucleation of new grains (Figure 9-Ia and 9-Ib). That is, during recrystallization after the initial heavy deformation many grains nucleated internally from misorientations developed during deformation [37, 48, 54]. As an outcome, a much finer recrystallized grain size was obtained (Figure 9-I), but the grains were very greatly misoriented from the preferred lambda fiber (Figure 10-II). Such heavy in-grain nucleation is seen in the partially annealed material (Figure 29d) in a region with high local misorientations.

It was also found that the density of lower angle grain boundaries (misoriented less than 15^{o}) in the recrystallized structure was significantly higher, about 25%, compared to 2% found in a material with a random texture [109]. Similarly, a high density of low angle grain boundaries was previously reported in high purity columnar coarse grained Al-Fe-Si alloys after heavy reduction and recrystallization [110]. This development of a high density of lower angle boundaries seems a common result of recrystallization of heavily deformed metals with a very large initial grain size. The presence of high density of these low angle grain boundaries indicates that the material has a “strong memory” of its original grain orientations.

Despite the instability of the lambda fiber some recrystallized grains at or near the lambda fiber are still present after the initial heavy deformation and recrystallization (Figures 9-I and 10-II). It is important to have some of the near lambda fiber grains for the success of the *two* subsequent light rolling reduction steps, each followed by recrystallization, in recovering the lambda fiber texture (Figures 9-II,III and 10-III,IV).

During light deformation, the textures changed little. However it is expected that significant differences in stored energy, associated with different orientations, were developed. The recovery of the preferred lambda fiber grains during subsequent recrystallization indicates that nuclei were formed on the existing high angle grain boundaries by SIBM growth of low stored energy lambda grains into adjacent grains with high stored energies. The idea that lower Taylor factors give lower stored energies [18], appears to be supported by the present modeling and nanoindentation results. The success of this working hypothesis in restoring the lambda fiber textures was supported by the critical test reported here that a *second* light deformation and recrystallization processing step further strengthened the desired lambda fiber texture.

The recrystallized grain size results given in Table 2 were initially surprising. Although it is perhaps *not* surprising to find somewhat similar grain sizes in recrystallized material after 90% deformation and after the first 10% reduction since before the first reduction the as-cast grain size was huge and this appears to have offset the much larger deformation imposed. The usual results for recrystallized grain size, given in the empirical "Laws of recrystallization" [111] is that: (i) recrystallized grain size increases with higher initial grain size, at least for moderate deformations and (ii) the recrystallized grain size falls with higher imposed deformation. However, the significant

increase of recrystallized grain size after the *second* light rolling reduction compared to the first even though they had similar starting grain sizes was initially puzzling. On the other hand, with the previously established [18] influence of a lower Taylor factor giving less stored energy, and its additional success in this study, it is perhaps not surprising to find a new addition to the so called "Laws of recrystallization". This is, that when the starting texture has a lower mean Taylor factor then that can increase the resulting grain size, due to the reduction of stored energy (less driving force for formation of recrystallization nuclei).

The results shown in Figure 9 and Table 2 appear to require this idea that the starting texture can have a significant influence on the recrystallized grain size through the influence of the mean Taylor factor. The initial heavy deformation occurred in a structure with a very low mean Taylor factor from its very strong lambda fiber, the second deformation occurred in a material in which the low Taylor factor lambda fiber had been greatly weakened while the third deformation was applied to a material in which that fiber had been strengthened.

The predicted Taylor factor maps (Figure 12) using both Taylor and finite element models are in good agreement and they confirmed the low Taylor factor values for orientations at and near the lambda fiber. Taylor and finite element simulations of the lambda fiber stability (Figure 13) have shown that the lambda fiber is only partially stable and very quickly, even after 10% rolling reduction, the cube component tends to be weakened and rotated cube strengthened. Experimental and modeling results (Figure 14) confirmed the partial stability of the lambda fiber even during heavy deformation. Predicted rotations of the crystals during light deformation (Figure 13) are consistent with

those during heavy deformation (Figure 14). Much of the lambda fiber (mostly rotated cube, component common for both alpha and lambda fiber) is retained after heavy deformation (Figure 14b). Taylor model strengthened alpha fiber more and finite element model strengthened only the rotated cube. If started with a random initial texture, both models predicted formation of the alpha and gamma fibers for moderate plane strain compression, therefore, both models behaved sensibly in predicting the deformed texture of the initial lambda fiber [21, 22].

Novel nanoindentation methodology was developed for extracting information about stored energy through extraction of indentation yield strength from indentation stress-strain curves. This was made possible by defining indentation stress and indentation strain and finding effective point of contact between the sample and spherical indenter. Characterization of the elastic and post-elastic behavior of as-cast electrical steel has shown significant anisotropy that resulted in measurable variations of the effective indentation modulus and indentation yield strength (Table 3). Obtained values of the effective indentation moduli, grouped around three distinct crystallographic orientations {001}, {101} and {111}, are considerably different from the values of Young's moduli, however, they follow the same trend with the increasing values from {001} through {101} to {111} orientation [107, 112]. Extracted orientation dependence of indentation yield strength (indentation Taylor-like factor) have also shown an increasing trend from {001} through {101} to {111} orientation.

Some of the indentation stress-strain curves from the as-cast state (figure 18b) exhibited pop-ins (linear increase in indentation stress followed by sudden increase in indentation strain and sudden drop of indentation strain). Typically, in the as-cast

structures the dislocation density is low and it is believed that dislocation-free regions were probed under the indenter and as a result starvation of dislocation is believed to occur during initial loading which caused increase in indentation stress. Once the dislocations (and dislocation sources) in the vicinity of the indentation site sensed the indentation stress a burst or avalanche of dislocations is believed to occur which caused both large indentation strain (large displacement) and sudden drop in indentation stress.

Indentation yield strength surface is generated from experimental values in order to extract indentation Taylor-like factors for new orientations developed during deformation. This allowed extraction of an increase in indentation yield strength after deformation due to an intrinsic increase in dislocation density (stored energy).

From the plane strain compression experiment to true strain of 1.6 it was possible, by using developed nanoindentation methodology, to extract the orientation dependence of stored energy (Eq. 5.5)) in term of difference in indentation yield strength at the grain-scale level. Crucial result is the lowest value of indentation yield strength found in the part of the grain with the orientation close to lambda fiber (location 3), while in other parts of the grain with the orientations further away from lambda fiber indentation yield strength increased. This observation supported the previously stated hypothesis that lambda fiber oriented grains have low stored energy.

The extremely surprising result (Table 5) was that large strain hardening is observed in the indentation stress-strain curves (Figure 22) when compared with the plane strain compression curves (Figure 23a) where in the second and third deformation steps the strain hardening is insignificant due to dynamic recovery (even though partially increased by friction between the sample and fixture). It has been reported that the strain

hardening can be influenced by the change of deformation mode [113]. The change of deformation mode introduces a new set of dislocations (relative to the set of dislocations developed during prior deformation mode) which contributes to the increase in strain hardening. Derived Eq. (3.9) reveals the sensitivity of stored energy to not only the dislocation density but also to types of dislocations present in the structure. Another possibility is due to different nature of the deformation between the plane strain compression and nanoindentation, i.e. during the plane strain compression whole sample (volume) is deformed simultaneously, while during the nanoindentation the top layer is deformed first and underneath layers subsequently after some periods of time (Figure 34). It is believed that this allows triggering of the new sources of dislocation with the increase of the indentation depth that contributes to high strain hardening.

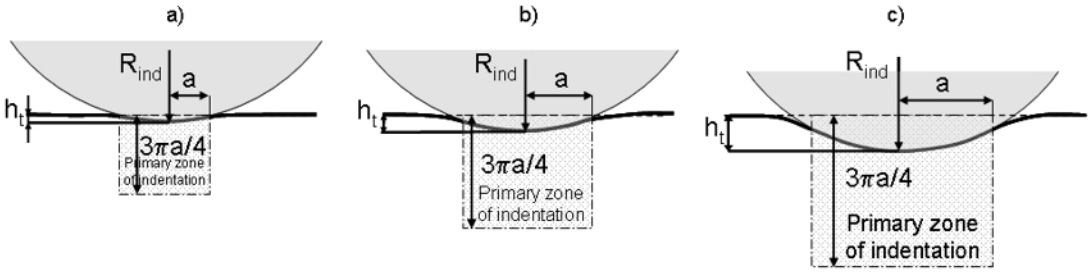

Figure 34: Sketch of the increase with time (left to right) of the primary indentation zone.

It is also observed that extracted indentation yield strength is 1.5-2 times larger than the plane strain compression yield strength. Possible explanation is in deformation mode, i.e. during nanoindentation the nanoindentation site is supported by surrounding material (all around and underneath) and plays a role in stress distribution, while during plane strain compression only two opposite sides of the sample are constrained by fixture.

During the first stage of plane strain compression to true strain of 1.21 the microstructure did not change significantly (Figure 24b). The initial lambda fiber was strengthened in a sense that misorientation from the ideal lambda fiber has decreased, but became less uniform because the rotations along the lambda fiber occurred which slightly weakened the cube component and slightly strengthened the rotated cube component (Figure 25-II). This is also in agreement with the predicted rotations of the crystals having the orientations in the vicinity of lambda fiber (Figure 13). Small rotations of the crystals contributed to an increase of in-grain misorientation from one to several degrees (Tables 6 and 7). The indentation yield strength (intrinsic increase in dislocation density) was substantial and relatively uniform between the all grains after the first deformation step (Table 7).

Even after the second stage of deformation the microstructure remained relatively homogeneous, except in grains no. 6 and 8 which show the first sign on variations in the orientation fields caused by different slip activity within the grains (Figure 24c). The overall texture evolution followed the same trend as previously observed in the first deformation stage. The rotated cube component has further strengthened with the development of alpha fiber while the simulation predicted more pronounced alpha fiber being developed by rotation of the crystals further away from the cube component (Figure 25-III). The in-grain misorientation has further increased to about 4^{o}, except in grain no.1 which had only a small increase in the in-grain misorientation. The indentation yield strength increased further after the second deformation stage and remained uniform between the grains (Table 8). Grain no. 6 had the largest increase in the yield strength.

After the third deformation step large misorientations were developed within the grains, except in grains no. 3, 7 and 8. Fragmented grains had mostly two deformation bands with the repeating orientation fields (Figures 24d and 26). Each of the split grains had deformation bands (labelled with A) with the <001> direction close to the compression direction. However, the newly evolved deformation bands in the split grains (except from the grain no.1) were developed by large rotations of the crystals away from both normal and rolling directions. The homogenous deformation bands in the split grains had their orientation fields closer to the cube orientation, while the grains that deformed homogeneously had orientations close to the rotated cube, which is known to be a stable orientation on rolling. This was reflected on the overall texture which had strong rotated cube and weak cube components. This result was also in a good agreement with the simulations (Figure 25-IV). It was not surprising to find that developed deformation bands had much higher indentation yield strength then their parent orientations from which they evolved. Deformation bands were formed by large local rotations caused by intensive slip that generated dislocations and increased the stored energy.

During the plane strain compression experiment columnar grains with the initial lambda fiber remained relatively stable and strain path average Taylor factor values did not change much from the initial values during monotonic plane strain compression. In order to establish correlation between the stored energy and Taylor factor the extraction of stored energy values is needed for the various orientations with the wide range of Taylor factor values.

In the plane strain compression experiment to true strain of 1.6 slightly higher flow stresses were achieved than in the plane strain compression experiment to true strain

of 1.2 although the strain hardening was miniscule in both experiments (Figure 23). This is probably caused by somewhat higher friction in the former experiment.

Developed local variations in stored energy and orientations at the grain-scale level have played an important role for nucleation and growth of recrystallized grains during partial annealing of deformed sample in a channel die. Annealing at 620^{o}C for 30 minutes lead to about 10-15% recrystallized microstructure. As expected the preferential nucleation occurred along the primary grain boundaries (Figure 30b). In addition, nucleation also occurred in the regions within the grain (top-left corner) and in the well recovered regions (as isolated islands).

Lastly, using nanoindentation technique it was possible to obtain the indentation stress-strain curves from several recrystallized grains, however, pop-ins were present during the initial loading (Figure 31). In addition smaller pop-ins and somewhat larger values of the indentation yield strength and flow stress were observed in the well recovered regions 3 and 5 since the dislocation density in those regions was larger (Figure 31). In the well recovered regions 1, 2 and 4 the pop-ins were not observed probably due to large enough dislocation density such that indentation sites were not free of dislocations (Figure 32). As a result the extracted indentation yield strength values were higher because of the large dislocation density (stored energy) still present in those regions.

CHAPTER 7: CONCLUSIONS

1) In this study it was shown that preferred texture for highly efficient AC motors, formed by directional solidification but lost during heavy rolling and recrystallization, could be recovered by applying multiple light rolling and recrystallization processing steps.
2) It was confirmed that the initially strong lambda fiber texture in the as-cast steel was partially stable during heavy rolling. Though greatly weakened by subsequent recrystallization, it was not completely destroyed.
3) Deformation of the very large grain sized starting material produced a fine grain structure with multiple grains arising from within individual starting grains, with a high density of low angle (less than15°) boundaries.
4) Application of two light rolling reductions each followed by recrystallization lead to very significant strengthening of the preferred lambda fiber texture.
5) The proposed hypothesis for this successful thermomechanical processing was that lambda fiber grains have low Taylor factors, associated with low stored energies. As a consequence, lambda fiber texture is strengthened by the Strain Induced Boundary Migration (SIBM) mechanism during recrystallization after applied light deformations.
6) An observation was made regarding a new “rule of recrystallization”, for controlling the recrystallized grain sizes. A starting texture with low average Taylor factors promotes a coarser grain size. The explanation for this new effect is the reduction of stored energy in material for a given applied strain due to reduced total slip.

7) A new nanoindentation methodology has been developed for converting the load-displacement data into indentation stress-strain curves. This involved a novel method for finding the effective zero-load and zero displacement point in the raw load-displacement data and the use of the Continuous Stiffness Measurements (CSM) data.
8) Combining OIM and nanoindentation techniques, evolution of the heterogeneous microstructure during compression in a channel die was characterized at the grain-scale level in terms of local orientations and stored energies.
9) It was confirmed that the initially strong lambda fiber texture in the as-cast steel was very stable up to moderate strains and only during the last deformation step grain fragmentation occurred. The differences in stored energy were quantified at the grain-scale level in term of increase in indentation yield strength.
10) From limiting number of completed experiments on samples with the columnar grain structure the proposed relationship between the Taylor factor and stored energy is not clear enough because the stored energy values are extracted for the very small range of Taylor factor values due to partial stability of initial lambda fiber.
11) Possible explanation for the large strain hardening observed in the indentation stress-strain curves is that the rate of generation of new dislocations is dependent on the dislocation density alone while the rate of annihilation of dislocation is strongly dependent on both dislocation density and the type of dislocations being generated (Eq. 3.10). It seems that later can be affected by changing the deformation mode.
12) An observation was made in partially annealed microstructure where local variations in stored energy and misorientations lead to heavy in-grain nucleation of the very first recrystallized grains captured at the onset of recrystallization.

CHAPTER 8: SUGGESTIONS FOR FUTURE WORK

1) To take advantage of the potential energy savings made possible by the processing developed in this thesis there is a vital need for twin roll cast electrical steel with an initial lambda fiber, ideally with the fine grain size.
2) Optimization of the develop processing by replacing heavy rolling by two moderate rolling steps with the recovery step in between. This may give lambda fiber a better chance to retain its strength during deformation and after subsequent recrystallization.
3) It is suggested to apply developed experimental methodology on deformed materials with initial random (or close to random) texture to correlate the stored energy with the wide range of Taylor factor values for more diverse orientations.
4) Another suggestion is study of dynamic recovery as a mean of existing dislocations and new dislocations generated and canceled out during continuous deformation to various strains and for different deformation modes from changes in strain hardening.
5) It is also suggested to study static recovery in terms of stored energy and subsequent formation of recrystallization nuclei and evolution of final recrystallized microstructure from well recovered structure with lowered stored energy.
6) In order to understand the deformation and recrystallization processes of the grains inside material it is suggested to use split sample where one half of the sample is a single crystal and the other half is a polycrystal with equiaxed grain structure.
7) Finally, to develop a numerical model that accounts for orientation dependence of the stored energy (yield stress) at the grain-scale level and try to predict grain rotation. Future understanding of the recrystallization process can be achieved by development of more accurate deformation models from now available new experimental data.

List of References

1. Cullity, B.D., *Introduction to Magnetic Materials*. 1972: Addison-Wesley. p. 515.
2. Bozorth, R.M., *Ferromagnetism*. 1st ed. 1951, New York: Van Nostrand. 572.
3. Goss, N.P., Trans. Metall. Soc. AIME, 1935. **23**: p. 511-544.
4. Honda, K. and S. Kaya, Sci. Rep. Tohoku Imperial University, 1926. **15**: p. 721.
5. Rollett, A.D., et al., Metall. Trans. A, 2001. **32A**(10): p. 2595-2603A.
6. Tesla, N., AIEE Transactions, 1888. **5**: p. 305.
7. Bessemer, H., US Patent 49053, 1865.
8. Yun, M., et al., Mat Sci Eng A, 2000. **280**: p. 116-123.
9. Mizoguchi, T. and K. Miyazawa, ISIJ International, 1995. **35**(6): p. 771-777.
10. Mccurrie, R.A., *Ferromagnetic Materials – Structure and Properties*. 1994, London: Academic Press.
11. Verlinden, B., et al., *Thermo-Mechanical Processing of Metallic Materials*. 2007: Elsevier, UK. p. 435.
12. Fisher, H.J. and J.L. Walter, Trans. Metall. Soc. AIME, 1962. **224**: p. 1271.
13. Flemings, M.C., *Solidification Processing*. 1974: McGraw-Hill, Inc. USA. p. 159.
14. Kurz, W. and D.J. Fisher, Acta Metall., 1981. **29**: p. 11-20.
15. Landgraf, F.J.G., et al., J. Magn. Magn. Mater., 2003. **254-255**: p. 364-366.
16. Yonamine, T., et al., Steel resch int, 2005. **76**: p. 461.
17. Dillamore, I.L., et al., Metal. Sci., 1968. **1**: p. 193.
18. Dillamore, I.L., et al., Proc. R. Soc. Lond. A., 1972. **329**: p. 405.
19. Beck, P.A. and P.R. Sperry, J. Appl. Phys., 1950(21): p. 150.
20. Inokuti, Y. and R.D. Doherty, Texture of Crystalline Solids, 1977. **2**: p. 143-168.
21. Hutchinson, W.B., Acta Metall., 1989. **37**(4): p. 1047-1056.

22. Samajdar, I., et al., Mat. Sci. and Eng., 1997(A238): p. 343-350.

23. Barrett, C.S., Trans. Metal. Soc. A.I.M.E., 1939. **135**: p. 296.

24. Orowan, E., Nature, 1942. **149**: p. 643.

25. Malin, A.S. and M. Hartherly, Metal Science, 1979. **13**: p. 463.

26. Hatherly, M. and A.S. Malin, Met. Tech., 1979. **6**: p. 308.

27. Hansen, N., Mat. Sci. and Tech., 1990. **6**: p. 1039.

28. Bay, B., et al., Acta Metall., 1992. **40**: p. 205.

29. Barrett, C.S. and M.A. Massalski, *Structure of Metals*. 1966: McGraw-Hill.

30. Gotthardt, R., et al., Texture, 1972. **1**: p. 99.

31. Sachs, G., Z. Ver. Deu. Ing., 1928. **72**(22): p. 734.

32. Taylor, G.I., J. Inst. Met., 1938. **62**: p. 307-324.

33. Kalidindi, S.R., et al., J Mech Phys Solids, 1992. **40**(3): p. 537-569.

34. Kalidindi, S.R., J Mech Phys Solids, 1998. **46**(2): p. 267-271.

35. Van Houtte, P., et al., International Journal of Plasticity, 2002. **18**(3): p. 359-377.

36. Dawson, P.R., International Journal of Solids and Structures, 2000(37): p. 115.

37. Panchanadeeswaran, S., et al., Acta Mater., 1996. **44**(3): p. 1233-1262.

38. Kalidindi, S.R., et al., Proc. R. Soc. A, 2004. **460**: p. 1935-1956.

39. Inokuti, Y. and R.D. Doherty, Acta Metallurgica et Materialia, 1978. **26**(1): p. 61.

40. Faivre, P. and R.D. Doherty, Journal of Materials Science, 1979. **14**(4): p. 897.

41. Doherty, R.D., et al., Acta Metallurgica et Materialia, 1993. **41**(10): p. 3029-3053.

42. Samajdar, I. and D. Doherty, Acta Materialia, 1998. **46**(9): p. 3145.

43. Doherty, R.D., Recrystallization of Metalic Materials, editor F. Haesnner, Dr. Riederer-Verlag Gmbh Stuttgart, 1978.

44. Cahn, R.W., J. Inst. Met., 1949(76): p. 121.

45. Cottrell, A.H., Prog. Metal Phys., 1953: p. 4.

46. Dillamore, I.L., et al., Met. Sci. J., 1967. **1**: p. 49-54.

47. Doherty, R.D. and J. Szpunar, Acta Metall., 1984(32): p. 1789-1798.

48. Doherty, R.D., et al., Mater. Sci. Eng. A, 1997. **238**: p. 219-274.

49. Dillamore, I. and H. Katoh, Metal Sci, 1974. **8**: p. 73.

50. Doherty, R.D. and R.W. Cahn, J Less Common Metals, 1972. **28**(2): p. 279-296.

51. Doherty, R.D., Metal Sci. J., 1974. **8**: p. 132-142.

52. Beck, P.A., Advances in Physics, 1954. **3**: p. 245-324.

53. Martin, J.W., et al., *Stability of Microstructure in Metallic Systems*. Cambridge Univeristy Press, Cambridge. 1997.

54. Humphreys, F.J. and M. Hatherly, *Recrystallization and Related Annealing Phenomena*. 1st ed. 1995, Oxford: Pergamon Press.

55. Bellier, S.P. and R.D. Doherty, Acta Metall et Mater, 1977. **25**(5): p. 521-538.

56. Haessner, F., R-Verlag, Stuttgart, 1979.

57. Beck, P.A. and H. Hu, Trans AIME, 1952(194): p. 83-90.

58. Dillamore, I.L. and W.T. Roberts, Met. Rev., 1965. **10**(39): p. 271.

59. Doherty, R.D., et al., Mat Sci Eng A, 1998. **257**(1): p. 18-36.

60. Jensen, D.J., Scripta Metallurgica et Materialia, 1992. **27**: p. 533-538.

61. Jensen, D.J., Acta Metallurgica et Materialia, 1995. **43**: p. 4117.

62. Doherty, R.D., et al., 16th Riso International Symposium, Denmark, 1995.

63. Hall, E.O., Proc. Phys. Roy. Soc., Ser. B, 1951. **64**: p. 747-753.

64. Petch, N.J., Iron and Steel Institute, 1953. **174**: p. 25-28.

65. Cahn, R.W., North Holland Publ. Comp., Amsterdam, 1965.

66. Davies, P.W., Instituiton of Metallurgists review course on Grain Control, Inst. of Metallurgists, London, 1969: p. 1.

67. Doherty, R.D., et al., In Aluminum Technologies-1987 (T. Sheppard ed.), The Institute of Metals, London, 1987: p. 289.

68. Hutchinson, W.B., Int. Met. Rev., 1984. **29**: p. 25.

69. Hutchinson, W.B., in Proc. ICOTOM 10, ed. Bunge, Clausthal, Trans Tech pubs., 1993: p. 1917.

70. Samajdar, I., et al., Acta Mater., 1998. **46**(8): p. 2751-2763.

71. Samajdar, I., et al., Acta Mater., 1999. **47**(1): p. 55-65.

72. Takashi, N. and J. Harasse, Mater. Sci. Forum, 1996. **204-206**: p. 143.

73. Lyudkovsky, G., et al., J. Metals, 1986. **22**: p. 18.

74. Hu, H., In: Thomas G, Washburn J, editors. Recrystallization by subgrain coalescence. Electron Microscopy and Strength of Crystals, New York, Interscience., 1963: p. 564-573.

75. Hu, H., Transactions of the Metallurgical Society of AIME, 1962. **224**: p. 75.

76. Bailey, J.E. and P.B. Hirsch, Proc Roy Soc London, 1962. **267**(1328): p. 11-30.

77. Lücke, K. and K. detert, Acta Metallurgica, 1957. **5**(11): p. 628-637.

78. Ferran, G.L., et al., Acta Metallurgica, 1971. **19**(10): p. 1019-1029.

79. Samajdar, I. and R.D. Doherty, Sripta Metall et Mat, 1995. **32**: p. 845.

80. Doherty, R.D., et al., Scripta Metall et Mat, 1992. **27**: p. 1459.

81. Bhattacharyya, A., et al., International Journal of Plasticity, 2001. **17**(6): p. 861.

82. DeHoff, R.T., J. Microsc., 1983. **131**: p. 259.

83. Spowart, J.E., Scripta Materialia, 2006. **5**: p. 5-10.

84. Schmidt, S., et al., Science, 2004. **305**(5681): p. 229-232.

85. Jensen, D.J., et al., M. Today, 2006. **9**(1-2): p. 18-25.

86. Nye, J.F., *Physical Properties of Crystals*. 1969: Oxford Univeristy Press.

87. Bunge, H.-J., *Texture analysis in materials science. Mathematical Methods*. 1993, Göttingen: Cuvillier Verlag.

88. Adams, B.L., Ultramicroscopy, Proceedings of the 6th Conference on Frontiers in Electron Microscopy in Materials Science, Jun 4-7 1996, 1997. **67**(1-4): p. 11-17.

89. Wright, S.I., et al., Mat Sci Eng A, 1993. **160**: p. 229.

90. Meyers, M.A. and K.K. Chawla, *Mechanical Metalurgy: Principles and Applications*. 1984: Prentice-Hall, New York.

91. Hirche, P.B. (Ed.), Physics of Metals, Vol. 2. 1975, Cambridge: Cambridge University Press. p. 189.

92. Kocks, U.F., J Eng Mater Technol, (ASME-H), 1976. **98**: p. 76.

93. Basu, S., et al., J App Physics, 2006. **99**(6): p. 063501.

94. Barsoum, M.W., et al., Physical Review Letters, 2004. **92**(25 I): p. 255508-1.

95. Murugaiah, A., et al., Journal of Materials Research, 2004. **19**(4): p. 1139-1148.

96. Doerner, M.F. and W.D. Nix, J. Mater. Res., 1986. **1**(4): p. 601-609.

97. Oliver, W.C. and G.M. Pharr, J Materials Research, 1992. **7**(6): p. 1564-1580.

98. Oliver, W.C. and G.M. Pharr, J Materials Research, 2004. **19**(1): p. 3-20.

99. Field, J.S. and M.V. Swain, J Materials Research, 1995. **10**(1): p. 101-112.

100. Herrmann, M., et al., Surface and Coatings Technology, 2006. **201**: p. 4305.

101. Hertz, H., *Miscellaneous Papers*. 1896, New York: MacMillan and Co., Ltd.

102. Li, X. and B. Bhushan, Materials Characterization, 2002. **48**: p. 11-36.

103. Field, J.S. and M.V. Swain, J Materials Research, 1993. **8**(2): p. 297-306.

104. Pathak, S., et al., Journal of the European Ceramic Society, 2008. **In print**.

105. Kalidindi, S.R. and S. Pathak, Acta Mat., 2007. **Submitted**.

106. Mencik, J. and M.V. Swain, Journal of Materials Research, 1995. **10**: p. 1491.

107. Vlassak, J.J. and W.D. Nix, Philosophical Magazine A, 1993. **67**(5): p. 1045.

108. Iordache, V.E., et al., Mat Sci Eng A, 2003. **359**: p. 62.

109. Mackenzie, J.K. and M.J. Thompson, Biometrika, 1957. **44**: p. 205.

110. Doherty, R., et al., Materials Science Forum, 2004(467-470): p. 843-852.

111. Burke, J.E. and D. Turnbull, Progress in Metal Physics, 1952. **3**: p. 220-292.

112. Sander, D., Rep. Prog. Phys., 1999. **62**: p. 809-858.

113. Rauch, E.F., et al., Acta Materialia, 2007. **55**: p. 2939

Appendix

For grain boundary characterization nanoindentation measurements were done in rows with shallow angle across grain boundary between grains no.1 and no. 2 (Figure 17). Indentation modulus and indentation yield strength are extracted from the load-displacement data in respect to distance from the grain boundary (Figure 35). It is interesting to notice that values for indentation moduli (figure 35a) in the grain no. 1 (<001> orientation) remained almost constant with the decreasing distance from boundary, while in the grain no. 2 (<111> orientation) values monotonically decreased with the decreasing distance from boundary. Indentation yield strength values (Figure 35b) remained almost constant with the change of the distance from boundary in grain no.2. while in grain no.1 indentation yield strength increased as the distance from boundary decreased. It is believed that elastic stresses are distributed across grain boundary instead of accumulated and that grain boundary can act as a prolific source of dislocations since no increase in hardening (yield strength) is observed across boundary. This is in contrast to the Hall-Petch theory and needs further investigation. It is possible that indentation sites were not close enough to boundary to observe Hall-Petch effect.

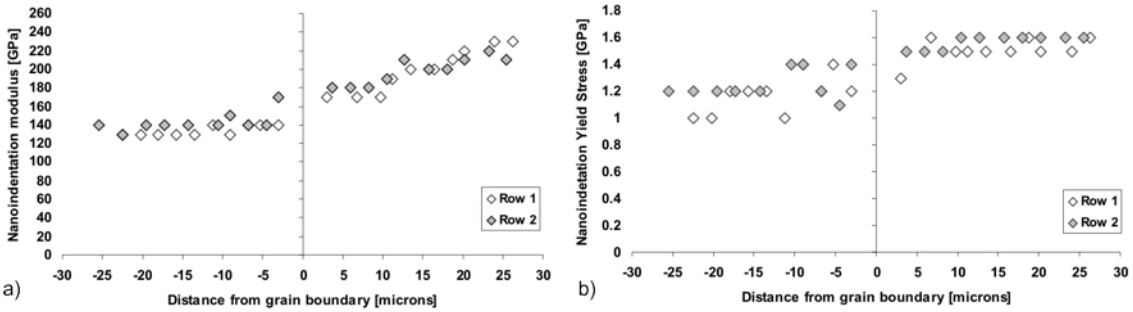

Figure 35: Extracted values for indentation moduli and indentation yield strength across grain boundary between grain no.1 (on the left side) and grain no. 2 (on the right side).

Vita

Name: Dejan Stojakovic

Birth: Subotica, Serbia, April 13th, 1974.

Education:

- Ph.D. Materials Science and Engineering, Drexel University, Philadelphia, PA, USA. 2008.
- B.Sc. Mechanical Engineering, Manufacturing, University of Novi Sad, Novi Sad, Serbia, 2000.

Experience:

- Graduate Research Assistant, Department of Materials Science and Engineering, Drexel University, 2003-2008.
- Graduate Teaching Assistant, Department of Materials Science and Engineering, Drexel University, 2004, 2006, 2007.
- Graduate Mentor, Research experience for undergraduates, DREAM and STAR summer programs, Department of Materials Science and Engineering, Drexel University, 2006, 2007.
- Lab Manager, Laboratories for sample preparation and mechanical testing, Department of Materials Science and Engineering, Drexel University, 2004-2008.
- Research Assistant, Materials Testing Laboratory, University of Novi Sad, 2000-2001, 2002-2003.
- Teaching Assistant, University of Novi Sad, 2000-2001, 2002-2003.

Honors:

- Dragomir Nicolitch Scholarship for leadership and exemplary grades - GPA 4.00, 2005-2006, 2006-2007, 2007-2008.
- Excellence in Teaching Award, Drexel University, 2006.
- Best Poster Award, ASM International®, Liberty Bell Chapter, 2005.
- Honorary Mention, Drexel Research Day, 2005.

Affiliations:

- Student Board Member, ASM International®, Liberty Bell Chapter, 2006-2007.
- Student Member, Materials Advantage (TMS, ASM international®, AIST, ACerS), 2004-2008.